AD-A276 835

RE

Form Approved
OMB No. 0704-0188

Public reporting burden for this collection of information is estimated to average 1 hour per response, including the time for reviewing instructions, searching existing data sources, gathering and maintaining the data needed, and completing and reviewing the collection of information. Send comments regarding this burden estimate or any other aspect of this collection of information, including suggestions for reducing this burden, to Washington Headquarters Services, Directorate for Information Operations and Reports, 1215 Jefferson Davis Highway, Suite 1204, Arlington, VA 22202-4302, and to the Office of Management and Budget, Paperwork Reduction Project (0704-0188), Washington, DC 20503

1. AGENCY USE ONLY (Leave blank)	2. REPORT DATE	3. REPORT TYPE AND DATES COVERED
	February 1994	Professional Paper

4. TITLE AND SUBTITLE	5. FUNDING NUMBERS
NONLINEAR DYNAMIC ANALYSIS OF FRANGIBLE NOSECAP FOR VERTICAL LAUNCH ANTISUBMARINE ROCKET (VLA)	PR: ZE84 PE: 060293N WU: DN309053

6. AUTHOR(S)

R. C. Shaw

7. PERFORMING ORGANIZATION NAME(S) AND ADDRESS(ES)

Naval Command, Control and Ocean Surveillance Center (NCCOSC)
RDT&E Division
San Diego, CA 92152-5001

94-07759

9. SPONSORING/MONITORING AGENCY NAME(S) AND ADDRESS(ES)

Office of Chief of Naval Research
OCNR-20T
Arlington, VA 22217

**DTIC
ELECTE
MAR 10, 1994
S B D**

11. SUPPLEMENTARY NOTES

12a. DISTRIBUTION/AVAILABILITY STATEMENT

Approved for public release; distribution is unlimited.

12b. DISTRIBUTION CODE

13. ABSTRACT (Maximum 200 words)

Described here is the application of a nonlinear finite element analysis (FEA) technique to predict the structural behaviors for a class of brittle materials that shows near-complete brittleness when loaded in tension, but exhibits some ductility when compressed. An ABAQUS* constitutive model, consisting of an isotropically hardening yield surface, which is active when the stress state is dominantly compressive, and an independent "crack detection surface" to determine if a point in the material fails by cracking in tension, is employed to simulate the failure of the brittle material. The application of the technique to determine if a potential frangible nosecap design of the Vertical Launch Antisubmarine Rocket (VLA) would break up as intended upon water impact for a given entry condition is presented as an example.

* ABAQUS is a FEA computer code that is a registered trademark of Hibbitt, Karlsson, & Sorensen, Inc.

14. SUBJECT TERMS		15. NUMBER OF PAGES
frangible nosecaps large deformation non-linear structural analysis water entry		
		16. PRICE CODE

17. SECURITY CLASSIFICATION OF REPORT	18. SECURITY CLASSIFICATION OF THIS PAGE	19. SECURITY CLASSIFICATION OF ABSTRACT	20. LIMITATION OF ABSTRACT
UNCLASSIFIED	UNCLASSIFIED	UNCLASSIFIED	SAME AS REPORT

NSN 7540-01-280-5500

94 3 9 043

Standard form 298 (FRONT)

21a NAME OF RESPONSIBLE INDIVIDUAL	21b TELEPHONE (Include Area Code)	21c OFFICE SYMBOL
R. C. Shaw	(619) 553–3230	Code 893

Accession For

NTIS GRA&I	☑	
DTIC TAB	☐	
Unannounced	☐	
Justification		

By_____

Distribution/ ___.

Availability Codes

Dist	Avail and/or Special
A-1	

NONLINEAR DYNAMIC ANALYSIS OF FRANGIBLE NOSECAP
FOR VERTICAL LAUNCH ANTISUBMARINE ROCKET (VLA)

Rhett C. Shaw, Ph.D.

Naval Command, Control and Ocean Surveillance Center
Research, Development, Test and Evaluation Division
San Diego, CA 92152-5001
U.S.A.

ABSTRACT

Described here is the application of a nonlinear finite element analysis (FEA) technique to predict the structural behaviors for a class of brittle materials that shows near-complete brittleness when loaded in tension, but exhibits some ductility when compressed. An ABAQUS* constitutive model, consisting of an isotropically hardening yield surface, which is active when the stress state is dominantly compressive, and an independent "crack detection surface" to determine if a point in the material fails by cracking in tension, is employed to simulate the failure of the brittle material. The application of the technique to determine if a potential frangible nosecap design for the Vertical Launch Antisubmarine Rocket (VLA) would break up as intended upon water impact for a given entry condition is presented as an example.

INTRODUCTION

A conflicting design requirement was encountered in the design of frangible nosecaps for the VLA. To protect the sensitive nose of the payload, the nosecap must withstand the canister overpressure and the canister cover push-through load during firing, the maneuver and aerodynamic loads during the powered flight and the ballistic glide, and the airframe separation and parachute deployment loads during descending. The nosecap, however, must shatter and completely clear the nose of the payload during water entry. The launch and aerodynamic loads determined the ogival shape and the lower-bound thickness profile of the nosecap, but it remained a difficult task to determine if a potential nosecap design would break apart upon water impact. A nosecap that remained intact during water entry would render the payload useless. After several trial-and-error attempts to choose the right material, a glass-filled phenolic molding compound called the Fiberite FM 4005, was chosen. But lacking a potent analytical tool to determine the water-entry behavior of the nosecaps still hindered the design process. A computational technique called WEST[1,2] (Water Entry Structural Technique) was developed by Jung and this author in 1990 to assess the water-entry behavior of the frangible nosecaps for VLA. The technique links the powerful geometry and finite element model (FEM) pre and postprocessor PATRAN#, a potential-flow, finite difference computer code that can calculate dynamic pressure-time histories of an arbitrary water-entry body called ENTRY,[3] and the finite element analysis code ABAQUS. Through this linkage, the extremely cumbersome and error-prone problem associated with the manual application of large amounts of time-varying load data into ABAQUS FEA for the response calculation of the water-entry body was eliminated. Although somewhat successful in its initial application in assessing the potential frangible nosecap design for VLA, the calculation of the time-varying

---

pressure profiles of the nosecap that was based on the original (undeformed) shape of the nosecap and the use of maximum principal stress theory that was based on results of a linear stress analysis to determine the failure of the material, lacked the accuracy demanded for by the tight and restrictive design envelope inherent to the frangible nosecaps.

METHOD OF APPROACH

BRIEF DESCRIPTION OF WEST

WEST is a computational technique that integrates the load and response calculations for an arbitrary body impacting water. WEST utilizes the PATRAN FEM pre and postprocessor and several self-developed FORTRAN computer programs to provide an effective linkage between the potential-flow computer code ENTRY, which can calculate dynamic pressure-time histories of an entry body, and the ABAQUS FEA code. Figure 1 shows a simplified flow diagram of WEST. Besides using PATRAN for mesh generations of the FEM and the water-entry model (WEM) of the entry body and the graphical display of FEA results, three particular features of PATRAN utilized in this application are as follows:

1. PATRAN has the capability to output the geometry of a FEM (nodal definition and elemental connectivity) in an American Standard Code for Information Interchange (ASCII) neutral file. This file is then translated into the formatted input readable by the ENTRY code by a FORTRAN computer program written for this application, PATENTR.

2. PATRAN has the capability to accept a formatted ASCII file input containing the step-by-step loading on the elements of the entry body and display them graphically to ensure that the dynamic pressures calculated by ENTRY at each time-step are applied to the corresponding elements correctly in the ABAQUS FEA.

3. The neutral file format for the element loading required by PATRAN, as described above, is encoded into ENTRY as an added capability to output the element pressure-time history file readable by PATRAN.

IMPROVEMENTS ON WEST

To overcome the drawbacks encountered in the application of WEST for the rational design of frangible nosecaps for VLA, as pointed out in the introduction section, two significant improvements are made in the process of WEST. They are described in the following paragraphs.

Pressure-Time Histories Based on Deformed Geometry of Entry Body

The procedures to compute the pressure profiles for a deformed geometry of a water-entry body can be implemented effectively into the WEST process shown in Figure 1 as follows:

1. Monitor the deformation of the entry body step-by-step during the ABAQUS analysis run for the initial sets of element pressure-time histories that were computed upon the original, undeformed geometry of the body. This can be done easily since deformations and stresses can be written on file (filename.fil) one step at a time in ABAQUS and this file can be accessed and translated into filename_stp$i$.dis and filename_stp$i$.nod files by the ABAPAT

2

translator (a PATRAN module) to view the deformed shapes and stress distributions of the entry body at the end of ith step in PATRAN.

2. Halt the analysis temporarily when the deformation at the end of a certain time-step, say jth step, becomes significant. Superimpose the jth-step displacement file obtained in step 1 (filename_stp$j$.dis) onto the PATRAN neutral file of the original geometry (filename.neu) to form a formatted ASCII file (filename_stp$j$.neu) for the deformed geometry of the entry body. A FORTRAN computer program called DEFORMED.FOR was developed for this purpose. This step is necessary because PATRAN can take a formatted FEM input and plot the deformed shape of the model, but it cannot output the deformed geometry of the model, i.e., the nodal locations of the deformed mesh. Enter PATRAN and input the filename_stp$j$.neu file to view and verify the validity of the updated geometry of the WEM.

3. Run PATENTR to translate the deformed geometry at jth step into input (filename_stp$j$.lst) readable by ENTRY. Append the entry conditions for the remaining steps, such as the body orientation, entry velocity, wetting factor, and depth increment for the step, to filename_stp$j$.lst to form the complete input file (filename_stp$j$.in) for the updated WEM.

4. Run ENTRY to recompute the dynamic pressure profiles of the updated WEM for the remaining steps, starting from the end of the step at which the deformation was deemed significant. Provision was made in the existing ENTRY code to specify an initial body depth so that the pressures and forces at a particular depth can be determined without calculating the entire force-time histories from initial wetting of the body. This feature is fully realized here. Name the output file containing the pressure profiles starting from $(j+1)$th step the filename_stp$j$.pre.

5. Reenter PATRAN and input filename_stp$j$.pre to view the new sets of pressure profiles for the remaining steps and use ENTPRES to translate filename_stp$j$.pre into new sets of element pressure-time histories (filename_stp$j$.aba) readable by ABAQUS.

6. Update the remaining steps of element pressure-time histories in the ABAQUS input deck for restart (filename_stp$j$.inp) and restart ABAQUS to continue the response calculation. Restarting ABAQUS was made possible by the provision that loading and response histories for the prior steps were saved in a restart file (filename.res) and the loading histories can be redefined from one step to the other in a restart.

During the course of the analysis, these procedures are repeated as many times as necessary whenever the deformation changes significantly between time-steps.

Constitutive Model For Brittle Materials

The behavior of brittle meterials under tensile loads is characterized by its inability to undergo plastic deformation. A completely brittle material would fracture almost at the elastic limit, while a brittle metal, such as white cast iron, shows some slight measure of plasticity before fracture. The behavior of the nosecap material under tension falls somewhere in between. Unlike a ductile material in which yielding allows the material to redistribute localized stresses, these localized stresses continue to build up in a brittle material. Finally, a crack forms at one or more points of stress concentration, and it spreads rapidly over the section and fracture occurs suddenly.

3

The cracking and compressive behaviors of the frangible nosecap material that were simulated in the constitutive model in the analysis can be illustrated by the uniaxial response of a specimen shown in Figure 2a. The nosecap test coupon responses to the uniaxial tension elastically until an ultimate stress is reached. Cracks form and rupture follows almost immediately. In modeling, cracking is assumed to occur when stresses reach a failure surface, which is referred to as the "crack detection surface" in ABAQUS. This failure surface is defined as a linear relationship between the equivalent pressure stress, p, and the Mises equivalent deviatoric stress, q, that are defined in terms of the principal stresses as follows:

$$p = 1/3 \, (s_1 + s_2 + s_3), \text{ where } s_i, \, i = 1, 2, \text{ and } 3, \text{ are principal stresses, and}$$

$$q = \sqrt{3/2 \, (S_1^2 + S_2^2 + S_3^2)}, \text{ where } S_i = (s_i - p), \, i = 1, 2, \text{ and } 3, \text{ are stress deviators.}$$

Once a crack has been detected, its orientation is stored. Subsequent cracking at the same point is assumed to be orthogonal to this direction. The model is a smeared crack model in the sense that it does not track individual "macro" cracks. Instead, constitutive calculations are performed independently at each integration point of the finite element model. The presence of cracks enters into these calculations by the way in which the cracks affect the stress and material stiffness associated with the integration point. The postfailure behavior for direct straining across the cracks is modeled in ABAQUS with the "tension stiffening" option in which the retained tensile stress normal to a crack is a function of the deformation in the direction normal to the crack. Two types of "tension stiffening" are available in ABAQUS to specify the postcracking strain-softening behavior of the material: the STRAIN type and the DISPLACEMENT type. The postfailure stress-strain relationship is specified directly in the STRAIN type, as shown in Figure 2a, while the postcracking behavior is defined by specifying the displacement, u_o, at which a linear loss of strength after cracking gives zero stress in the DISPLACEMENT type. The first type has been used extensively in modeling the cracking behavior of the reinforced concrete. Crisfield[4] indicated, however, that too little "strain stiffening", as in the case of plain concrete, can introduce mesh sensitivity in the results such that the finite element predictions do not converge to a unique solution as the mesh is refined, because mesh refinement leads to narrower crack bands. He recommended Hilleborg's approach[5], the DISPLACEMENT-type tension stiffening approach, to allay this concern. This approach is based on a brittle fracture concept that the brittle behavior is characterized by a stress-displacement response rather than a stress-strain response, as shown in Figure 2b. The ultimate displacement, u_o, can be estimated from the fracture energy required to form a unit crack surface area, G_f, as $u_o = 2G_f/s^u_t$, where s^u_t is the ultimate tensile stress. This value sets an upper-bound limit on the specimen size so that the strain at failure, e^u_t, is less than the strain at the value of displacement, i.e., $e^u_t < u_o/L$, where L is the length of the specimen. For the analysis of the nosecap, the second approach is chosen and a value of $u_o = 0.002$ inch is used.

When the principal stress components are dominantly compressive, the response of the nosecap material is modeled by an elastic-plastic theory, using a simple yield surface written in terms of the equivalent pressure stress and the Mises equivalent deviatoric stress. Associated flow and isotropic hardening are used. In multiaxial stress states, these models are generalized through the concept of surfaces of failure and flow in the stress space. The surfaces used are shown in Figure 3a and 3b. The theoretical derivations of these surfaces are given in the ABAQUS Theory Manual.[6]

ANALYTICAL RESULTS

To illustrate the improved computational procedure implemented in WEST, a potential frangible nosecap design undergoing a 130-fps vertical water entry, which was analyzed,[1,2] was treated here as an example. As shown in Figure 4, this design features a plastic shell with a 1.25-caliber von Karman ogive. The shell is supported internally by four evenly spaced, blade stiffeners along the meridians. The blade stiffeners, made of a rigid, high-density polyvinyl foam material, are designed to carry the concentrated load caused by push-through of the canister cover during firing, to stiffen the shell against the flight loads, and to help breakup the nosecap when jammed against the metallic sidewall of the nose of the payload during water entry. The aft end of the nosecap is glued on with eight pieces of silicone rubber strips. These retaining strips are designed to allow the nosecap to slide on to the payload but to resist sliding off. The analytical results carried out by WEST consisted of plots of the nosecap FEM and WEM generated by PATRAN, the snapshots of pressure profiles during water entry computed by ENTRY, the element pressure-time histories plotted by YADAP,[#] the corresponding deformations, and the associated stress, elastic and plastic strain distributions of the nosecap computed by ABAQUS. Since the entire output of the dynamic analysis were bulky, only those for a few selected time-steps are presented here for brevity.

FEM AND WEM OF A FRANGIBLE NOSECAP DESIGN

Figure 5a shows the quarter-symmetric FEM of the potential nosecap design. The shell and the internal blade stiffeners were modeled with triangular and quadrilateral shell elements, except the tips of the stiffeners, which mate at the tip of the nosecap, were modeled with solid elements. The quarter-symmetric FEM took full advantage of the symmetric conditions for the geometry and loading of the nosecap entering water vertically. In generating the WEM for the calculation of water-entry loads, only the exterior surface of the shell needed to be modeled. The half-symmetric WEM of the undeformed nosecap is shown in Figure 5b. The model was constructed with quadrilateral, potential-flow elements, which were geometrically identical to and had the same elemental connectivities as the shell elements used in the FEM. It was due to this nature that PATRAN could be used to generate the WEM of the nosecap and display the pressure profiles of the nosecap during water entry. It should be noted that the only symmetry condition permissible by the current version of the ENTRY code is the half-symmetry.

Appropriate boundary conditions were applied in nosecap FEM to maintain the conditions of symmetry. For the load condition applicable to this investigation (symmetric radial loads), the retaining strips provide primarily radial resistance to shell displacement. Therefore, the strips were represented in the FEM by using radial single-point constraints for that portion of the shell retained by the strips. To allow the shell to slide over the aft ends of the blade stiffeners, radial and axial springs elements were attached in this region between the shell and blade-stiffener plate elements. The spring constants of these elements were selected to model the desirable displacements without adversely affecting the stiffness matrix of the FEM. The arched portions at the bases of stiffeners were restrained in axial direction since they were butted against the metallic surface of the nose of the payload.

YADAP is a PC computer code developed by D. Worth of Naval Surface Weapons Center, White Oak Laboratory, Silver Spring, Maryland.

PRESSURE PROFILES AND ELEMENT PRESSURE-TIME HISTORIES

Figures 6a to 6f show the pressure profiles of the nosecap undergoing 130-fps vertical entry during the time period of 0.0 and 3.113 milliseconds (ms). Note that only even time-steps after step 2 are shown for brevity. Figure 6a, at 0.045 ms after vertical entry, shows the tip of the nosecap (elements 1 through 8) fully wetted. The pressure, displayed at the centroids of the quadrilateral elements, rises sharply to 1791 psi. Figure 6b, at 0.177 ms after entry, shows pressure on the tip decaying rapidly to 271 psi, and pressure on the ring of elements 9 through 24 wetted with a pressure of 372 psi. Figure 6c, 0.844 ms after entry, shows the nosecap wetted to the upper edges of elements 41 through 56. The tip pressure has decayed to 150 psi, while the pressure on elements 9 through 24 has decayed to 108 psi, and the pressure on elements 41 through 56 has risen to 131 psi. By following Figures 6a to 6f, the progression of nosecap entry into water, as well as the progression of the pressure distribution up the nosecap can be seen. At Figure 6f, 3.113 ms after entry, shows the nosecap wetted to the upper edges of elements 137 to 152. The pressure has decayed from high 1791 psi at the tip, to a value of 36.7 psi around the ring of elements 105 to 120, and has not yet decayed to steady state along the upper ring of elements 137 to 152, which have just been wetted. The pressure peak has passed up the nosecap, while earlier-wetted elements have reached their steady state drag phase pressure profiles. Note that the pressure profiles of the nosecap for the steps 1, 2, and 4 were computed on the original nosecap geometry because of insignificant deformations at the early steps of the water entry, while the pressure profiles for steps 6, 8, and 10 were computed upon the updated geometry as the deformation became more significant in each step.

Figure 7 shows the pressure-time histories for the "rings" or "groups" of elements that experience the same pressure intensity during the vertical entry. Element group 1 consists of elements 1 through 8 on the tip, element group 2 is the ring of elements 9 through 24, element group 3 is the ring of elements 25 through 40, and so forth. These plots show, on elemental basis, how the pressure peaks at the later time the farther up the nosecap the element group is located, as well as the reduction in peak pressure the farther from the nosecap tip the element group is located. Element grouping is for computational efficiency only, not of necessity. An oblique entry would result in nonsymmetric loading and each element would have a unique pressure-time history throughout the water entry process.

PROGRESSIVE DEFORMATIONS

Figures 8a to 8f show the progressive deformations of the nosecap shell responding to the pressure profiles shown in Figure 6a to 6f. Despite the extreme pressure acting on the nose tip (Figure 6a) during the initial water impact, negligible deformation has taken place after the initial wetting shown in Figure 8a. Figure 8b, at 0.177 ms after entry, shows the beginning of deformation of the nosecap under the pressure distribution shown in Figure 6b. By following the progression from Figures 8c through 8f, the deformation of the nosecap in response to the pressure-time history can be clearly seen. Notice that a "hump" develops at the location of the shell interfacing with the blade stiffener, which is first visible in Figure 8d at 1.562 ms after entry. This radial extrusion was caused by the compressive force from the base of the stiffener created by payload nose's reaction to the drag force acting on shell during entry. As the radial extrusion becomes more severe at both support locations, a high bending moment is developed and causes the shell to bend inward into two circumferential waves between the two supports, as shown in Figure 8e. At the same time, the shell also bends inward along the center meridian between the two supports, as the side pressures become more dominant with the increasing of

6

shell's radius of curvature farther up the nosecap. These deformations become progressively more severe the further the nosecap is submerged, as shown in Figure 8f.

STRESS AND STRAIN DISTRIBUTIONS

The complicated deformation is associated with a rather colorful stress distribution at both inner and outer surfaces of the shell. Unlike a linear analyis in which stresses increase indefinitely with load, the stress distribution in an elastic-plastic analysis tends to "smooth" out as material points yield, fail and shed their loads to other material points before fracture. Figures 9a to 9b and 10a to 10b show distributions of the first (smallest) principal stress (s_1) and the third (largest) principal stress (s_3) for the inner and outer surfaces of the shell, respectively, at the last convergent solution-step before failure (step 10, $t = 3.113$ ms). As shown, the maximum first principal stresses, which are compressive, occur at the edge of the inner surface location of the shell interfacing with the aft end of the blade stiffener (node 118 in Figure 9a) and at the outer surface of the concavity along the center meridian (node 78 in Figure 10a). The maximum third principal stresses, which are tensile, occur either at the aft stiffener interface (node 136 in Figure 9b) or at the midspan between the fore and aft stiffener supports (node 73 in Figure 10b). At this stage, the material has already gone plastic. Figures 11a to 11c and 12a to 12c show the plastic strain distributions in the meridional, hoop and in-plane shear directions, respectively, at the inner and outer surfaces of the shell. As a stress component is a function of the strain components in all directions, as well as the history of loading in the plastic regime, it is difficult to interpret these complex stress states, let alone the effects caused by the presence of dynamic loads with associated moving stress waves and the possible participation by high-frequency shell responses. However, the plastic strain distributions shown in Figures 11a to 11c and 12a to 12c clearly reflect the deformation pattern shown in Figures 8e and 8f. The maximum tensile plastic strains in the meridional and hoop directions (e^P_{11} in Figure 12a and e^P_{22} in Figure 12b) and the maximum in-plane shear strains (e^P_{12} in Figures 11c and 12c), which are responsible for the fracture of the brittle material, occurred either at the concavities associated with the circumferential bending between the two stiffener supports or at the "humps" caused by the radial extrusion of the stiffeners.

FAILURE OF NOSECAP

Because the stress and strain states are basically biaxial in a thin shell, a plastic strain magnitude defined below is used as a measure of how much plasticity has taken place in the biaxial stress state:

$$PE_{mag} = \sqrt{(2/3)\ e^P_{ij}\ e^P_{ij}}\ ,$$

where e^P_{ij}, i, j = 1 and 2, are the plastic strain components. In expanded form,

$$PE_{mag} = \sqrt{2/3}\ [(e^P_{11})^2 + (e^P_{22})^2 + 2(e^P_{12})^2]^{1/2}\ .$$

Figures 13a to 13c and 14a to 14c show the time-history plots of PE_{mag} distributions between the onset of plastic deformation and the last convergent solution-step prior to failure for the outer and inner surfaces of the shell, respectively. As shown in Figure 13a, the plastic deformation corresponding to the extrusion of the blade stiffener described in Figure 8d starts at the outer surface of the shell supported by the blade stiffener at $t = 1.562$ ms (step 6), while the inner surface remains elastic. The inner surface does not go plastic until $t = 1.938$ ms

(step 7), with the maximum occurring at the concavities of the two waved circumferential bending described in Figure 8e. The plastic zones intensify and expand as the nosecap submerges deeper into water. Figure 15 shows the envelopes for the maximum values of PE_{mag} for outer and inner surfaces. It shows that the plastic deformations for both inner and outer surfaces increase sharply with time initially, but stay constant once the pressure loading has passed its peak. The plastic strains then rise again until failure occurs. To further substantiate this observation, the time-histories for the first and third principal stresses at the critical locations where their maxima occur, i.e., nodes 73, 78, 118 and 136, are plotted in Figures 16a and 16b, respectively. Since the first principal stresses are predominantly compressive and the third principal stresses tensile and that the ultimate tensile strength of the nosecap material (7,540 psi) is only one-fourth of its compressive strength (30,160 psi), the third principal stress is clearly the deciding factor in determining the failure of the nosecap. As shown in Figure 16a, the third principal stress at the inner surface of node 136 (the aft stiffener interface) oscillates periodically as the stress waves travel up the nosecap during the early stage of the water entry when the material remains elastic. But, the stress rises sharply and loses its periodicity once the plastic deformation begins at t = 1.563 ms (step 6). It reaches the ultimate tensile strength at t= 2.323 ms (step 8) and unloading follows afterwards. This indicates that cracks have formed and the DISPLACEMENT type tension-stiffening model ultilized in the analysis determines the postcracking behavior. However, the analysis continues for only two more time-steps before the solution ceases to converge, indicating that rupture has occurred.

CONCLUSIONS

In conclusion, the objective to improve the water entry structural technique for the rational design of frangible nosecaps for air- and surface-launched undersea weapons has been met. The calculations of pressure profiles that were based on the current, deformed geometry of the entry body would undoubtedly result in a more accurate prediction of the entry loads. This improvement can be more useful in the water-entry application where the entry body is made of ductile materials, because they can sustain more severe deformation before rupture occurs. Repetitions to update the deformed geometries before computing the water entry loads between time-steps become necessary.

The nonlinear dynamic analysis that employed a constitutive model capable of detecting initiations of tensile cracks for brittle materials is well-suited for the application to determine if a potential frangible nosecap design would break up upon water entry. Plastic strain magnitude predicted by the constitutive model employed in the FEA is a good indicator of failure for the brittle material used by VLA nosecaps. Under a 130-fps vertical entry condition for the proposed nosecap design shown in Figure 4, the analytical results indicated that the cracks would initiate at the inner surfaces of shell locations interfacing with the aft ends of the blade stiffeners. These cracks would spread out rapidly over the areas and fracture ensues quickly. The other high stress points for potential failure are: (1) the inner surfaces of the shell located about one- and three-fourth ways along the circumference between the two stiffener interfaces, and (2) the unsupported area about halfway up the nose tip along the center meridian between the two blade-stiffener supports.

REFERENCES

1. Jung, P. A. and Shaw, R. C., "Water Entry Structural Technique (WEST): An Analytical Technique to Determine Frangible Nosecap Behavior During Water Entry," NOSC Technical Report 1317, December 1990.

2. Shaw, R. C., "Water Entry Structural Technique (WEST): An Analytical Technique to Determine Frangible Nosecap Behavior During Water Entry," Proceedings, International PATRAN User's Conference, October 1991.

3. Wardlaw, A. B., Jr., A. M. Morrison, and J. L. Baldwin, "Prediction of Impact Pressure Forces and Moments During Vertical and Oblique Water Entry," Naval Surface Weapons Center, White Oak Laboratory Technical Report 77-16, January 1977.

4. Crisfield, M. A., "Snap-through and Snap-back Response in Concrete Structures and the Dangers of Under-integration," Int. J. Meth. Eng., vol. 22, pp 751-767, 1986.

5. Hilleborg, A., M. Modeer and P. E. Petersson, "Analysis of Crack Formation and Crack Growth in Concrete by Means of Fracture Mechanics and Finite Elements," Cement and Concrete Research, vol. 6, pp 773-782, 1976.

6. ABAQUS Theory Manual, Hibbitt, Karlsson & Sorensen, Inc., Version 5.2, pp 5.9.1-1 to 5.9.1-15, 1992.

IMPROVED WATER ENTRY STRUCTURAL TECHNIQUE (WEST)
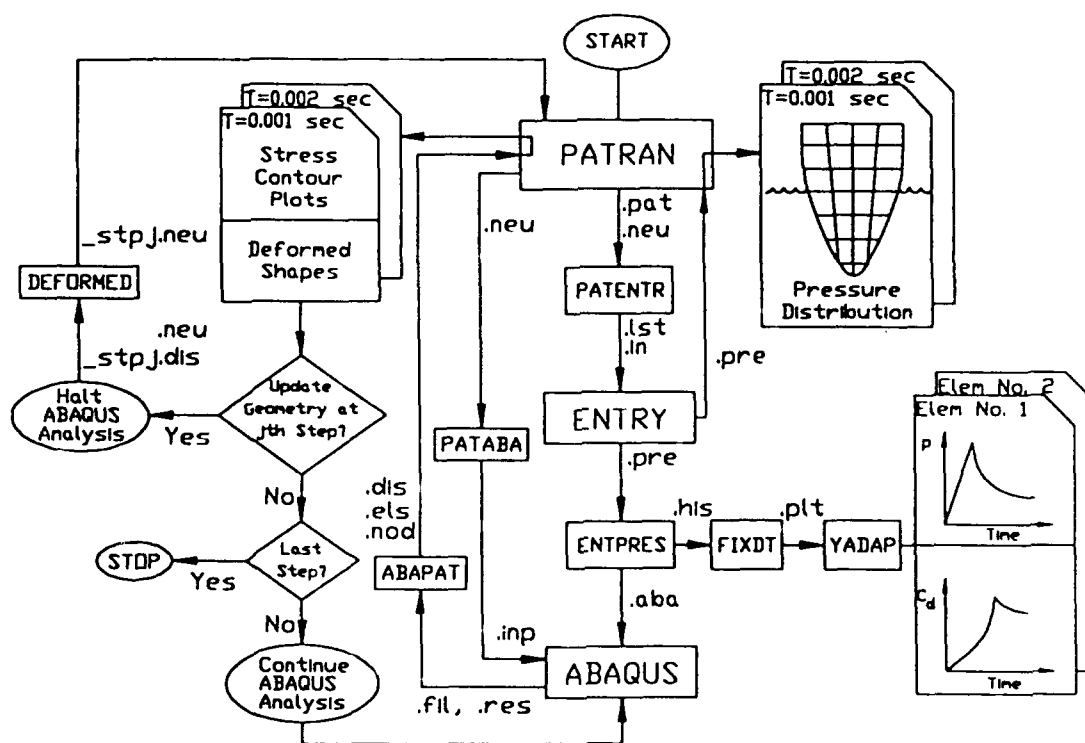
Figure 1. Simplified flow diagram of improved WEST.

Mechanical Properties of Glass-Filled Phenolic:

Young's Modulus $E = 2 \times 10^6$ psi, Poisson's Ratio = 0.28

	Compression	Tension
Yield	$\sigma^y = 17,100$ psi	
Ultimate	$\sigma_c^u = 30,160$ psi	$\sigma_t^u = 7,540$ psi
		uo = 0.002 inch
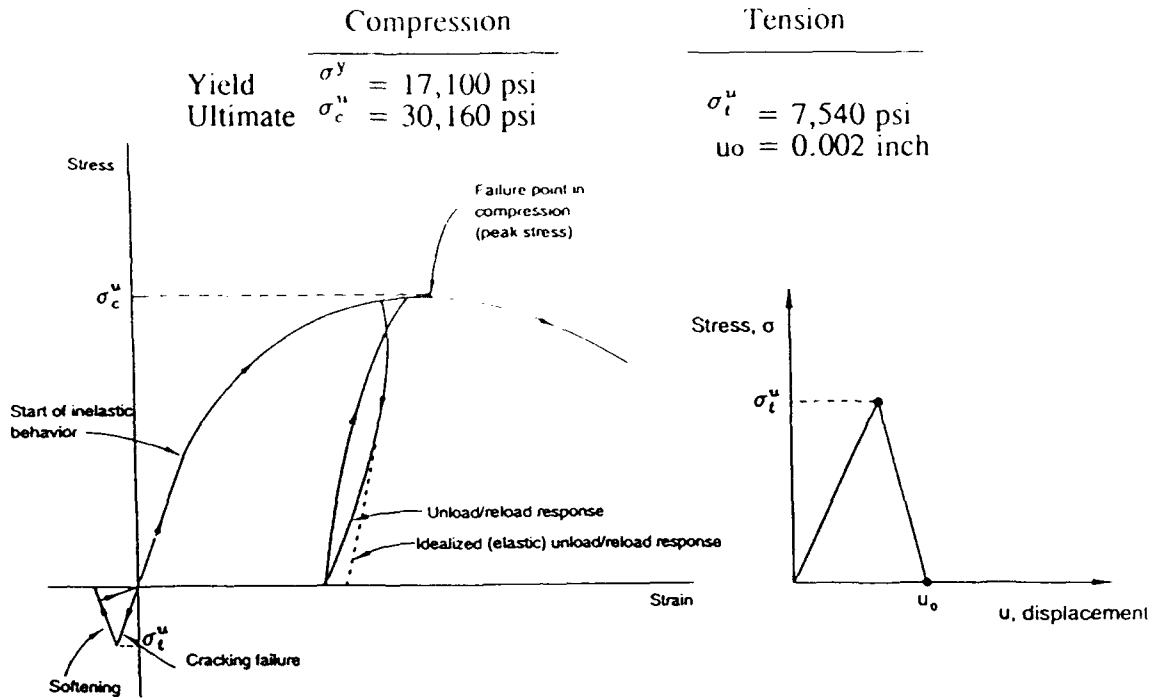
Figure 2a. Uniaxial behavior of brittle material.

Figure 2b. Fracture energy cracking model.
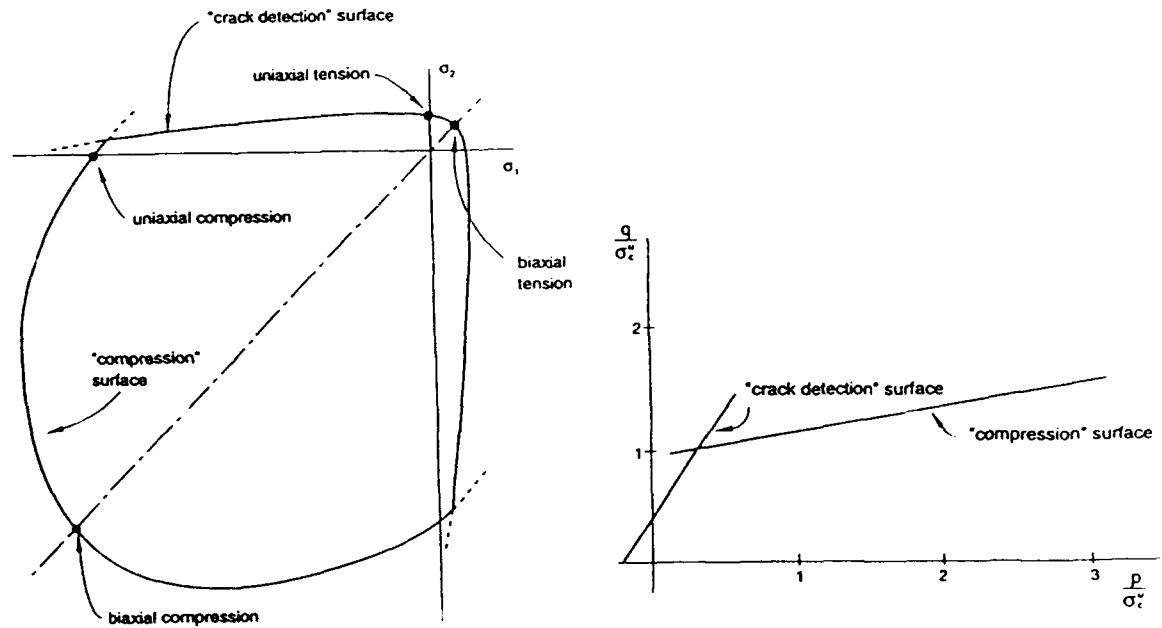
Figure 3a. Yield and failure surfaces in plane stress.

Figure 3b. Yield and failure surfaces in (p-q) plane.

Figure 4. A blade-stiffened, frangible nosecap assembly.

11
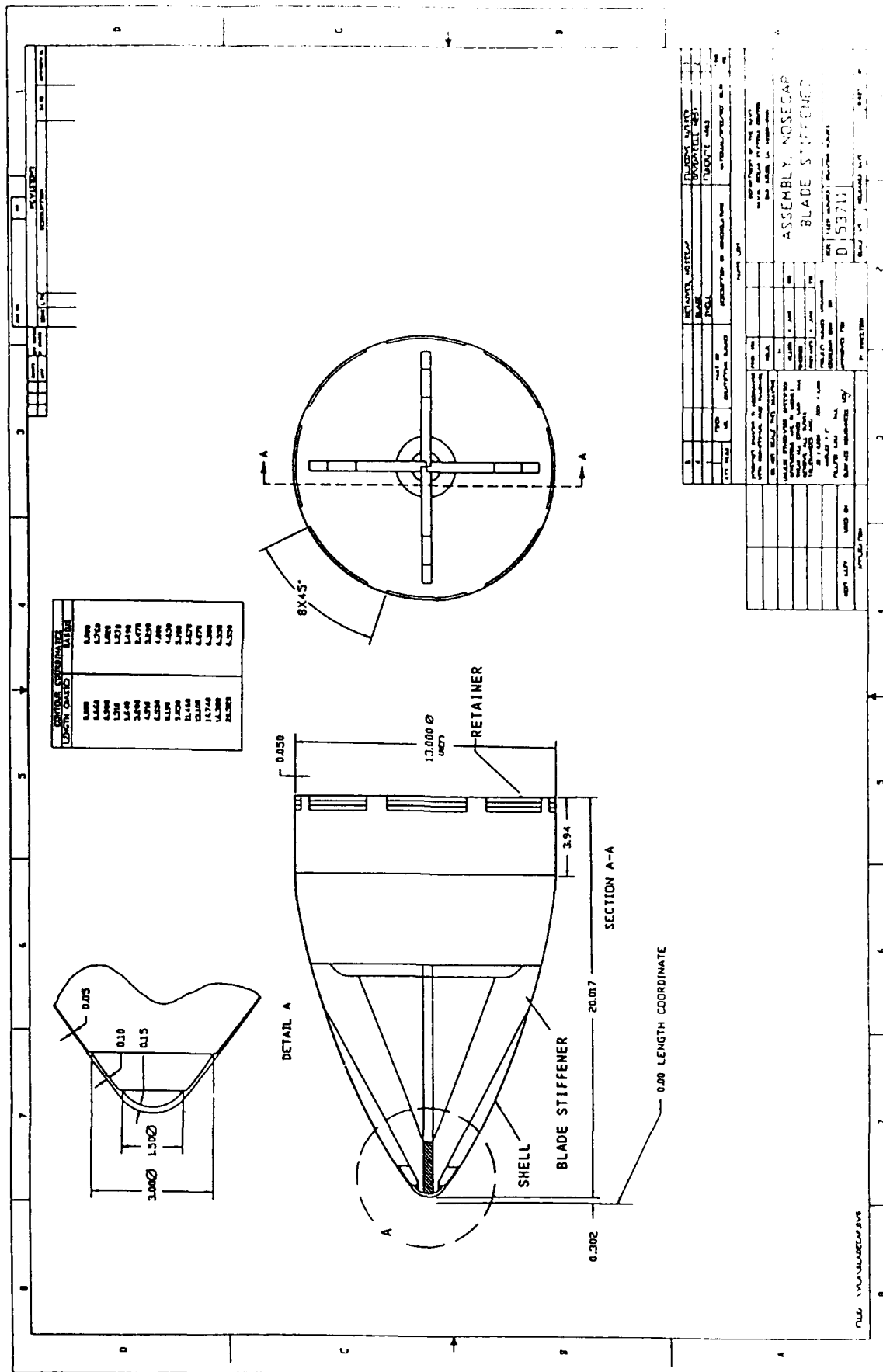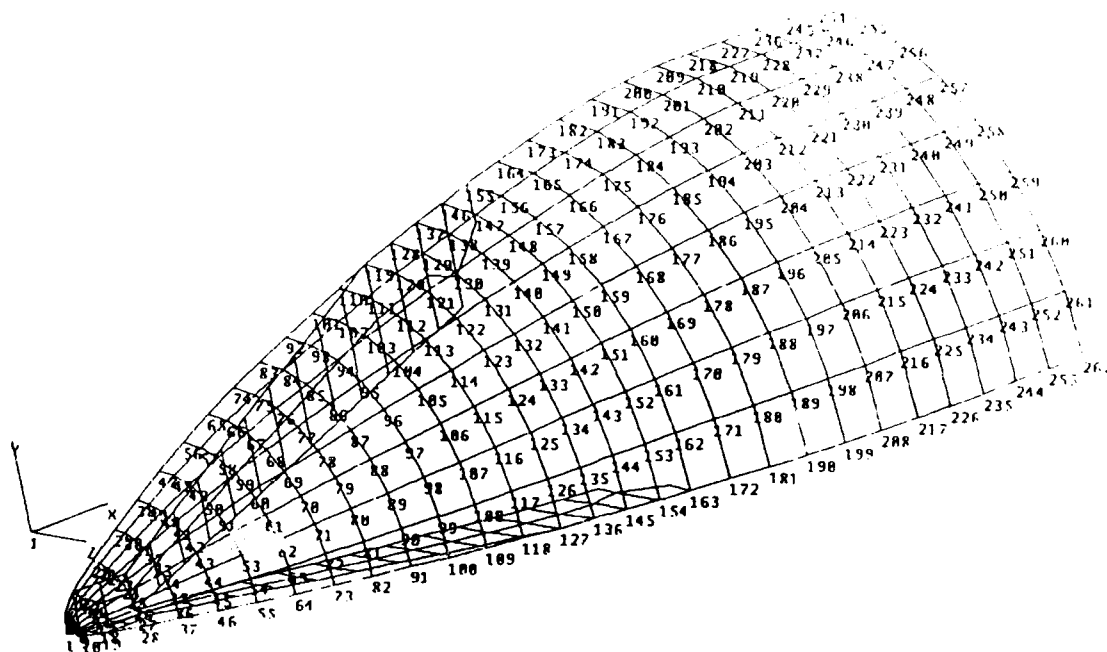
Figure 5a. Quarter-symmetric finite element model of blade-stiffened nosecap.
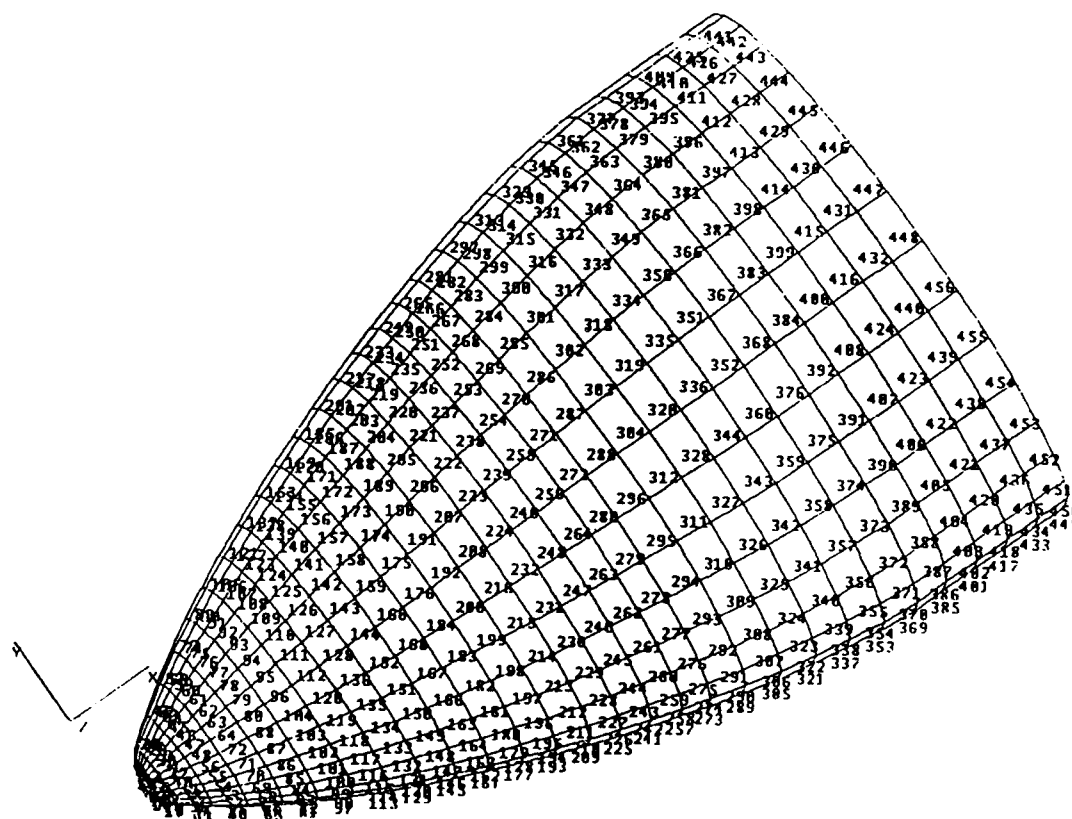
Figure 5b. Half-symmetric water-entry model of nosecap shell.
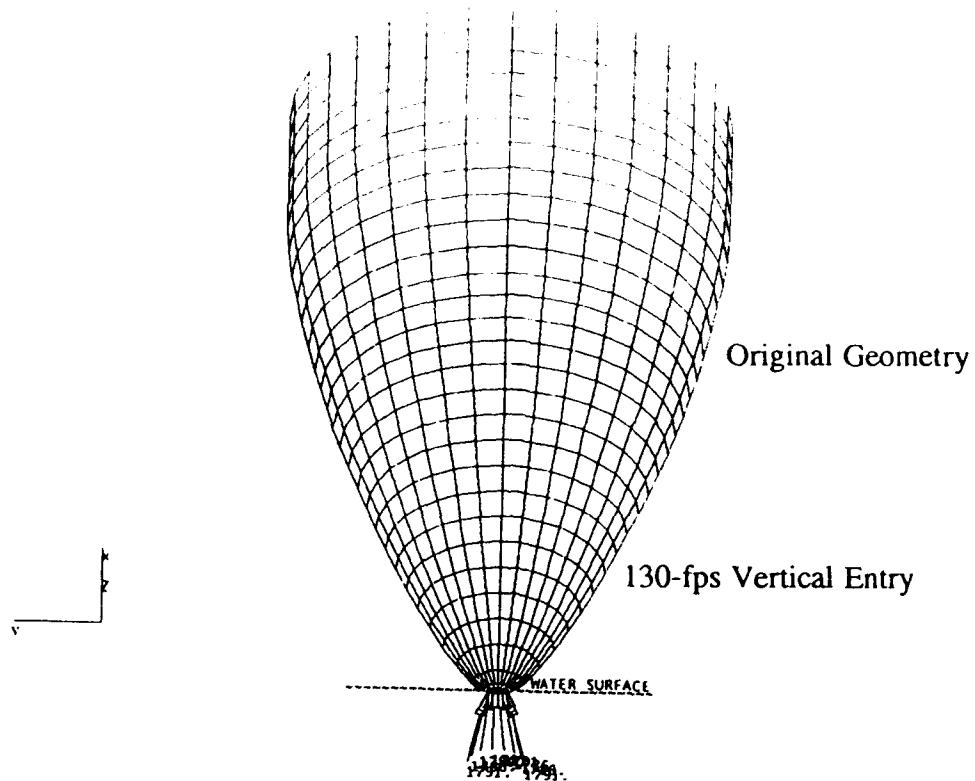
Figure 6a. Pressure profile of nosecap at t = 0.045 ms (step 1, initial wetting).
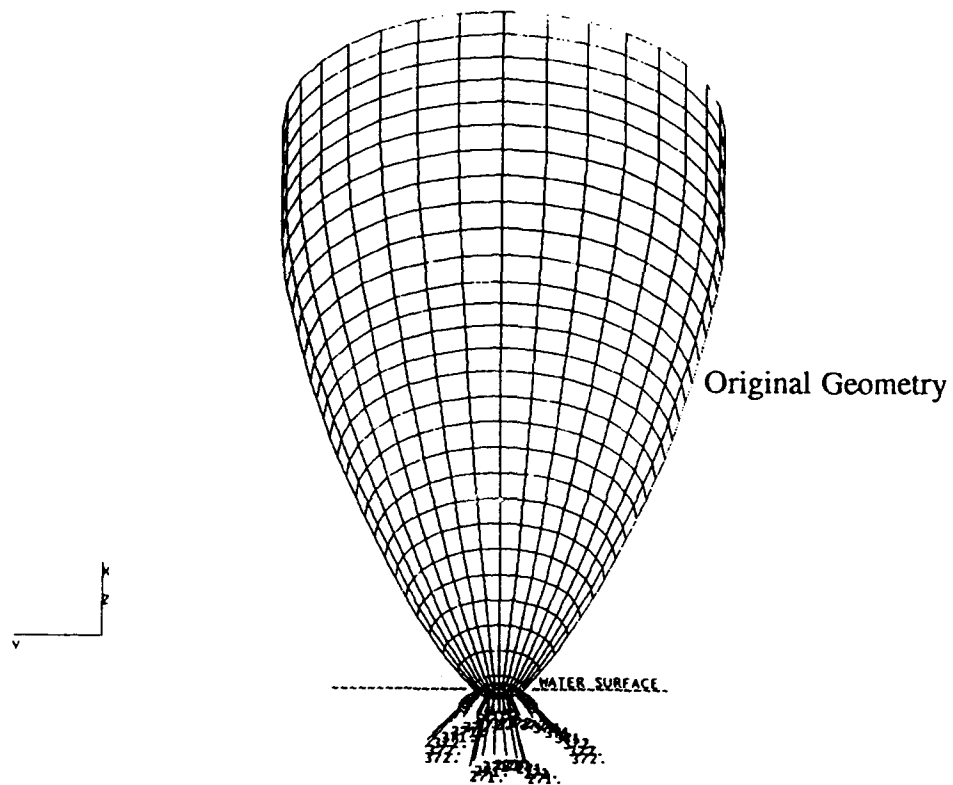
Figure 6b. Pressure profile at t = 0.177 ms (step 2).

Original Geometry
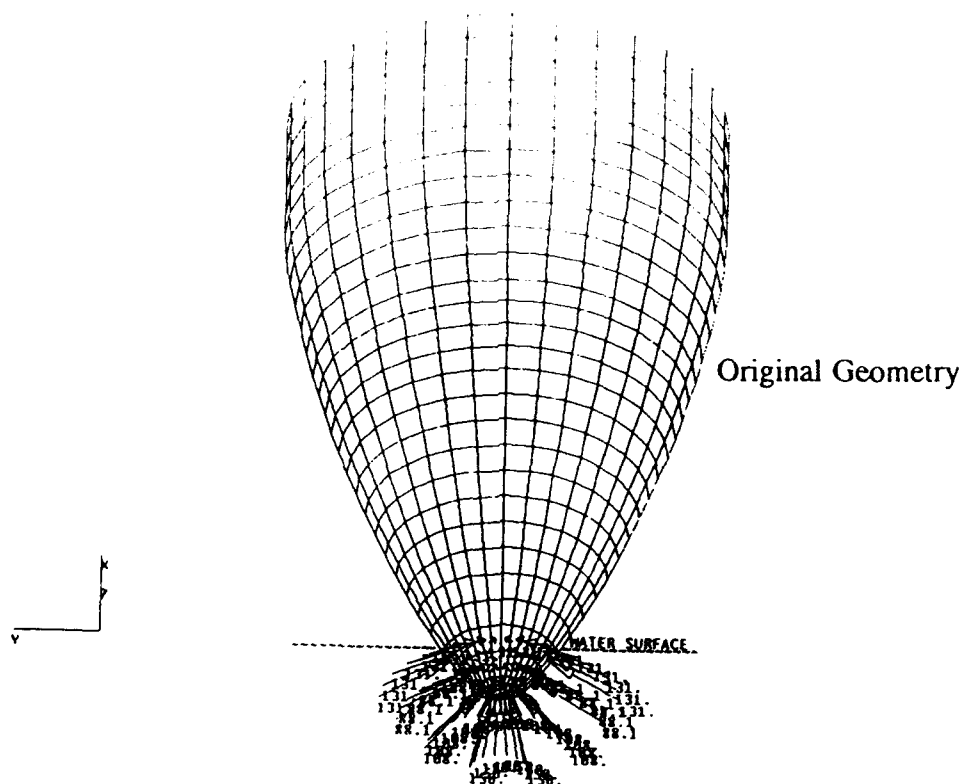
Figure 6c. Pressure profile at t = 0.844 ms (step 4).

Deformed Geometry
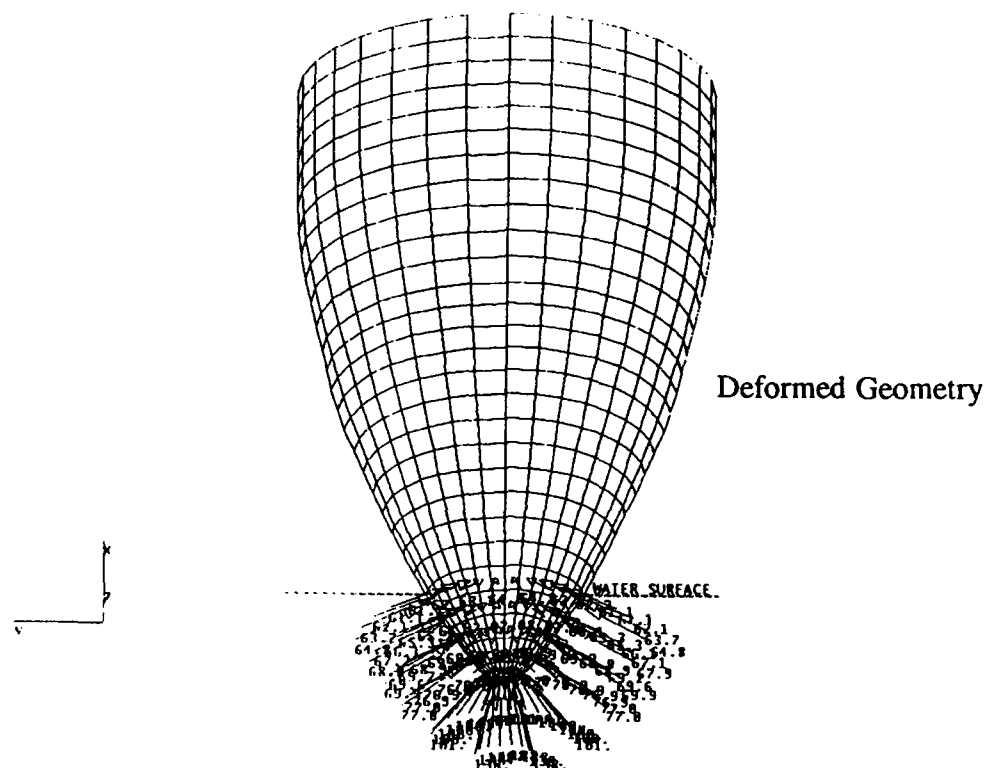
Figure 6d. Pressure profile at t = 1.562 ms (step 6).

14
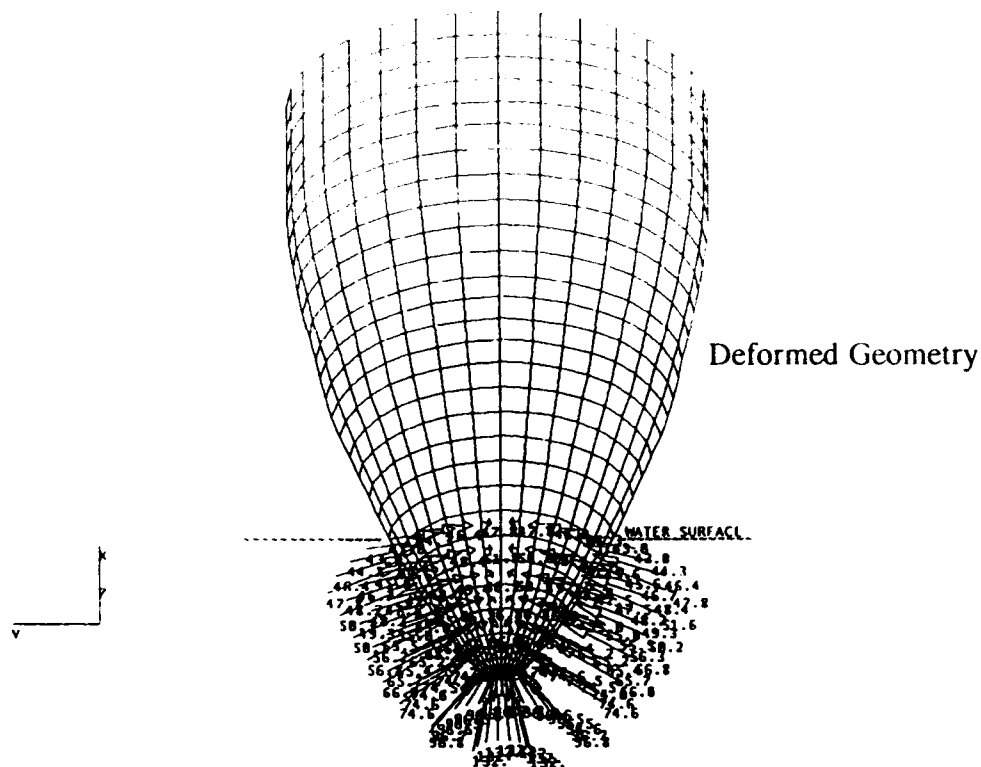
Figure 6e. Pressure profile at t = 2.323 ms (step 8).
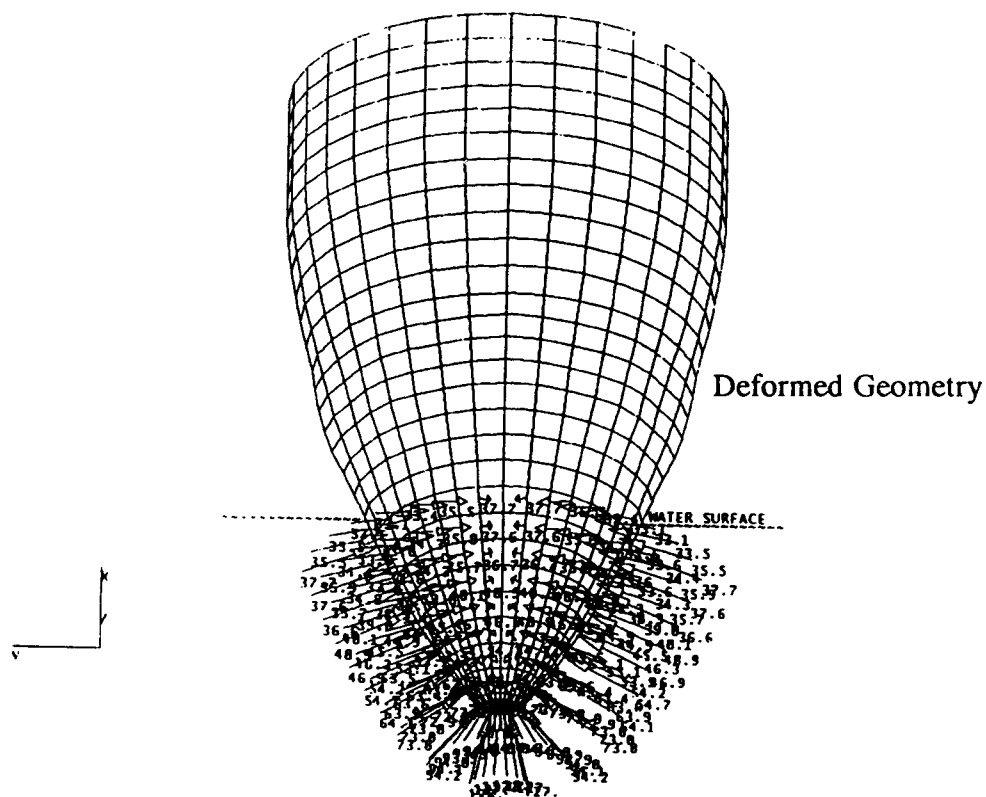
Figure 6f. Pressure profile at t = 3.113 ms (step 10).
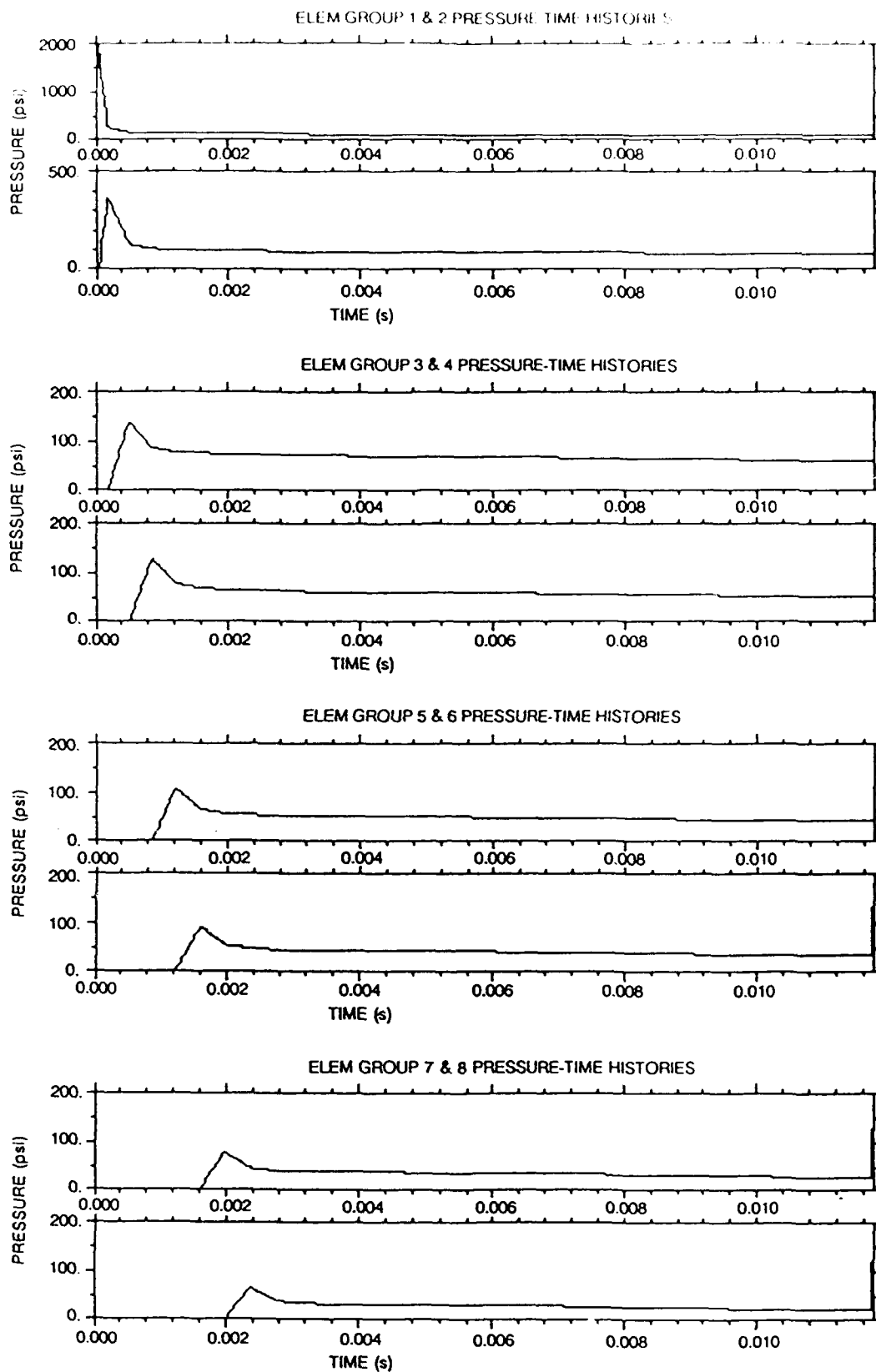
Figure 7. Element pressure-time histories (0.0 - 0.010 sec).
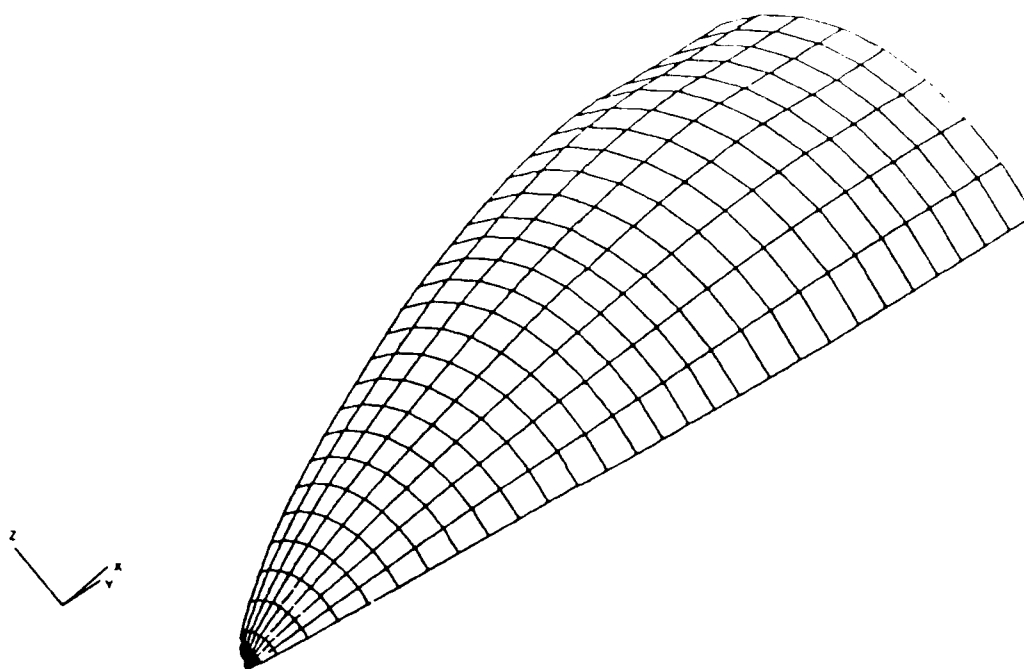
Figure 8a. Progressive deformation of nosecap shell at t = 0.045 ms (step 1, initial wetting).
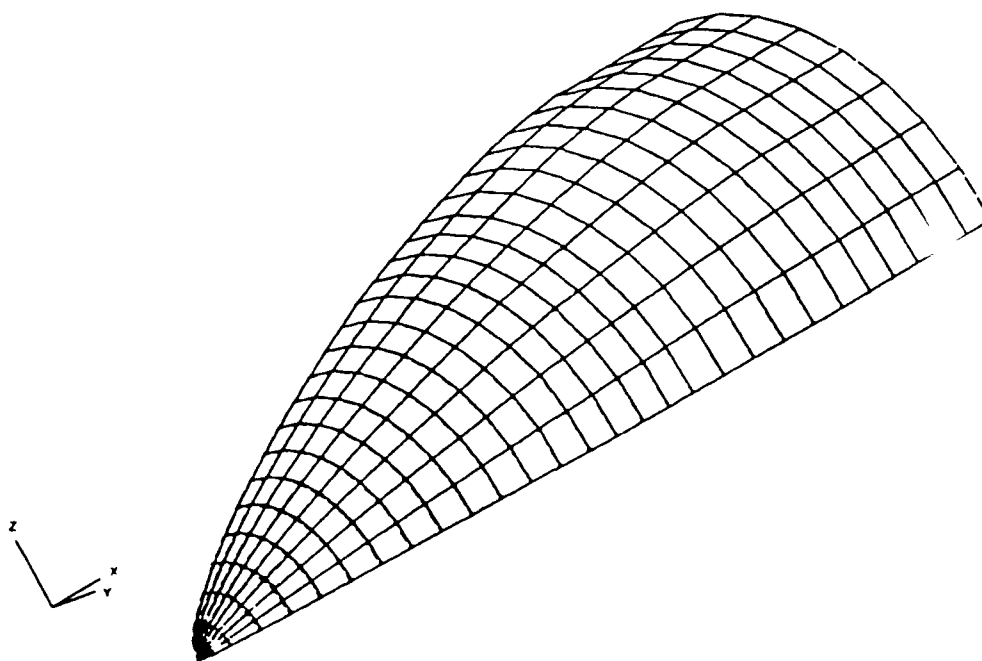
Figure 8b. Deformed shape of shell at t = 0.177 ms (step 2).
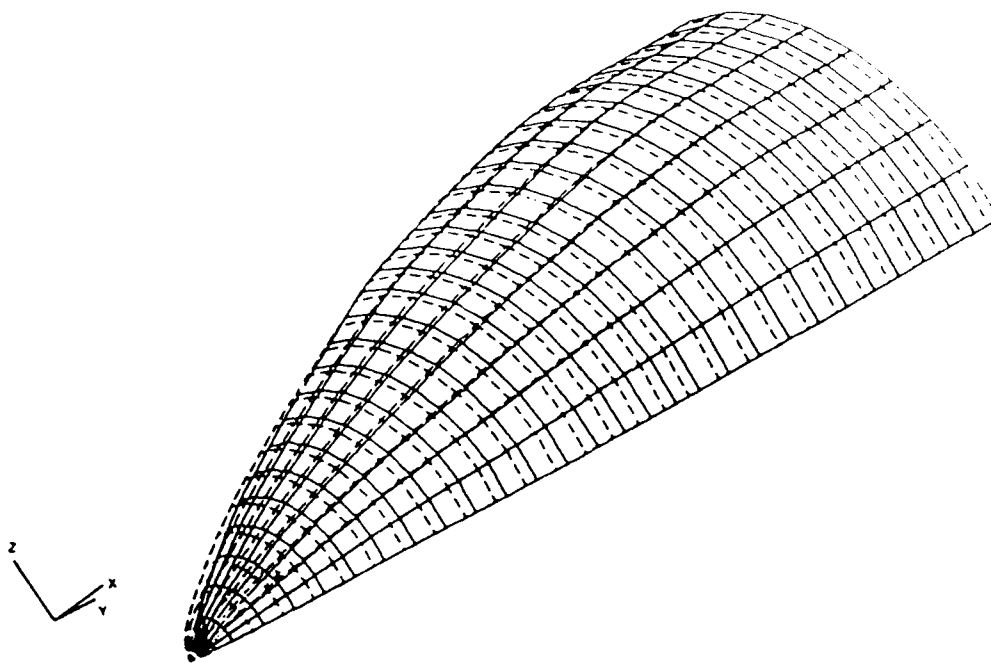
Figure 8c. Deformed shape of shell at t = 0.844 ms (step 4).
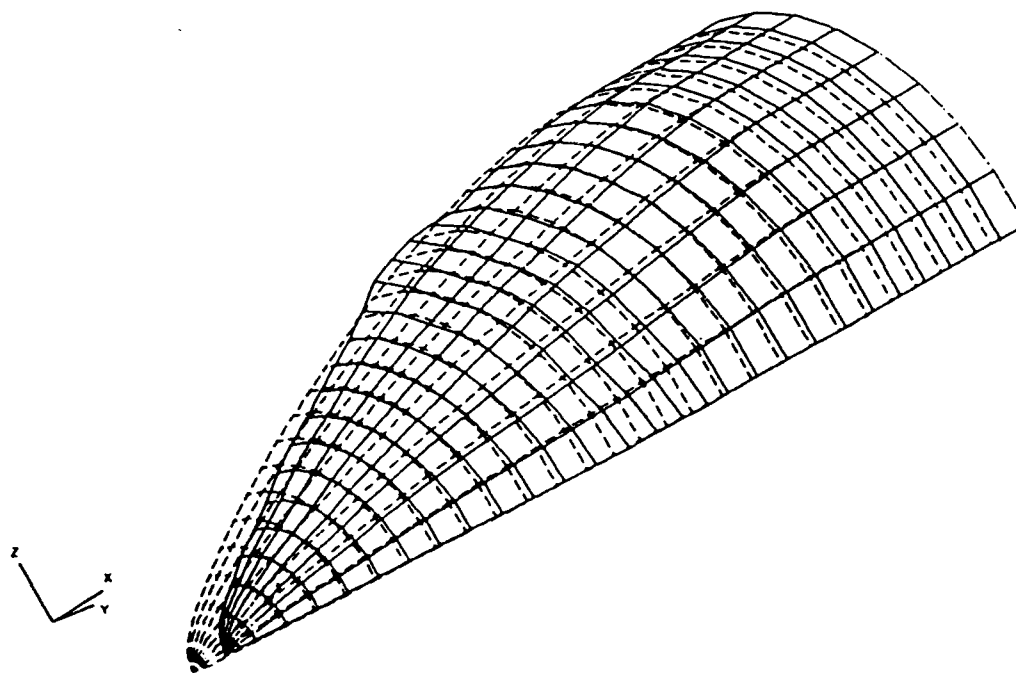
Figure 8d. Deformed shape of shell at t = 1.562 ms (step 6).
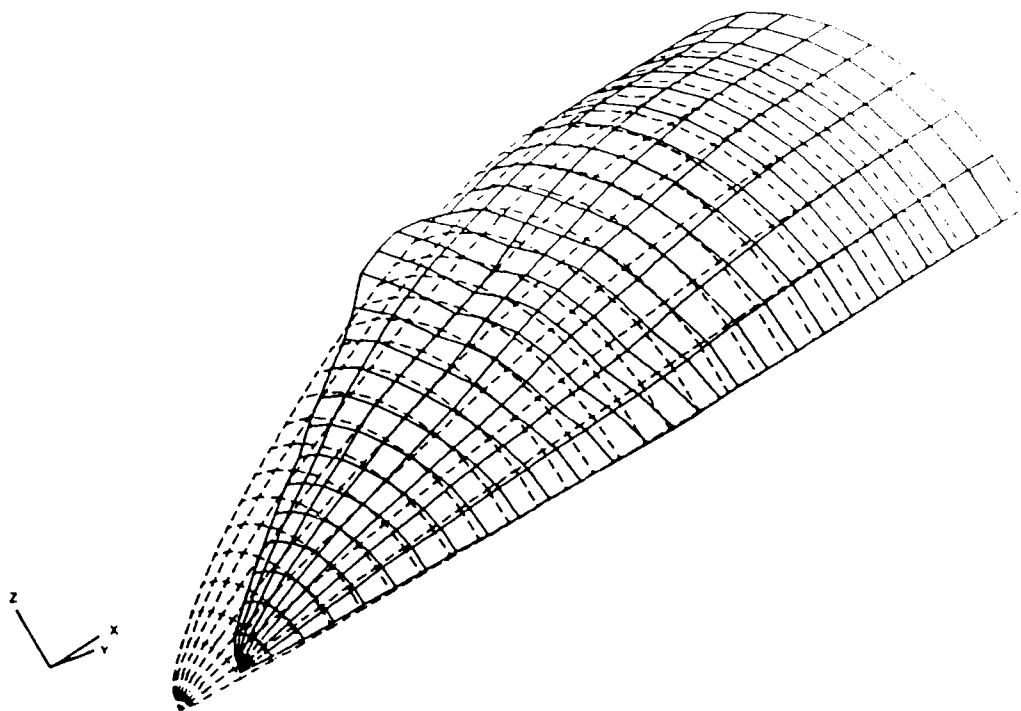
Figure 8e. Deformed shape of shell at t = 2.323 ms (step 8).
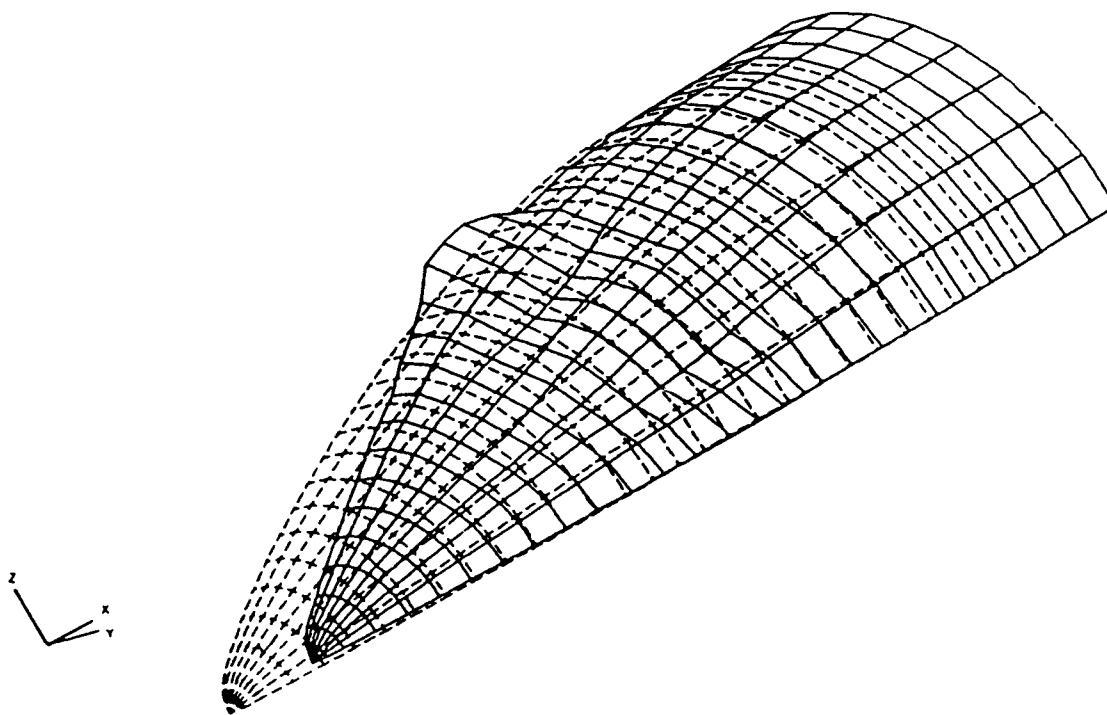
Figure 8f. Deformed shape of shell at t = 3.113 ms (step 10).
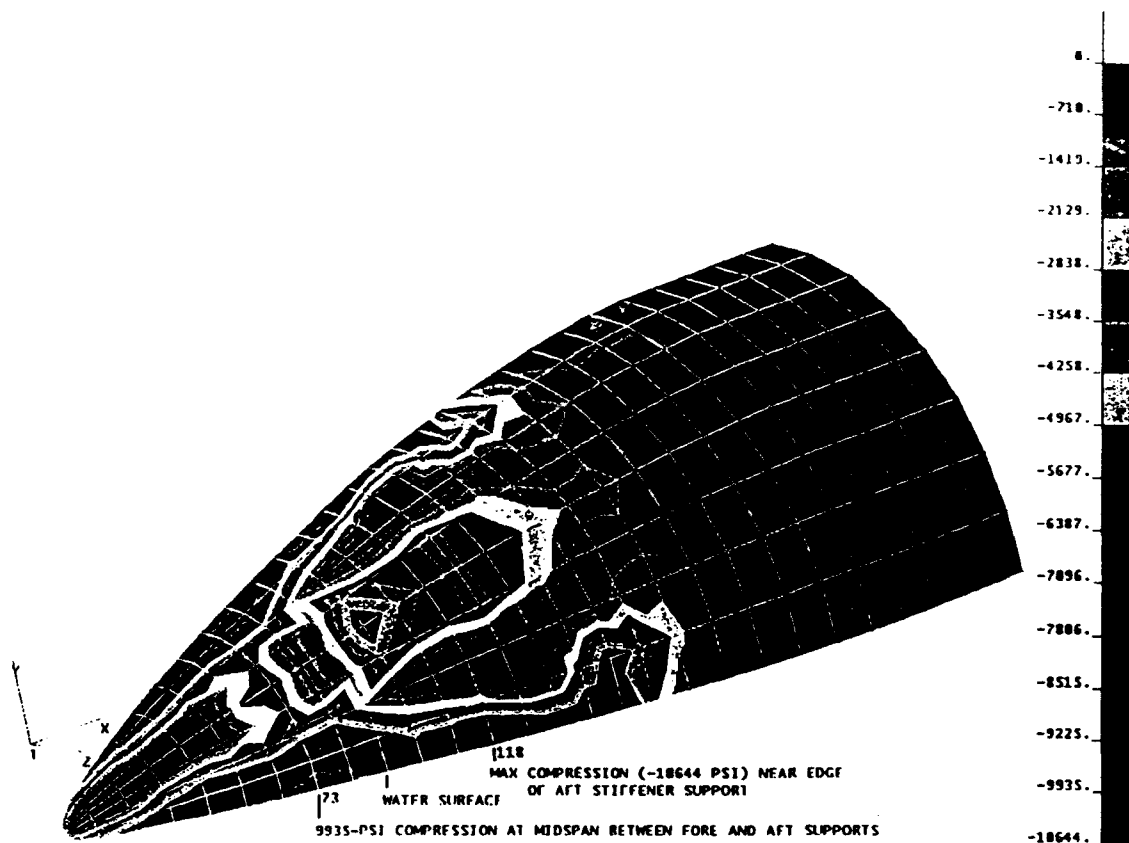
Figure 9a. First principal stresss (s_1) of inner surface at t= 3.113 ms (step 10).
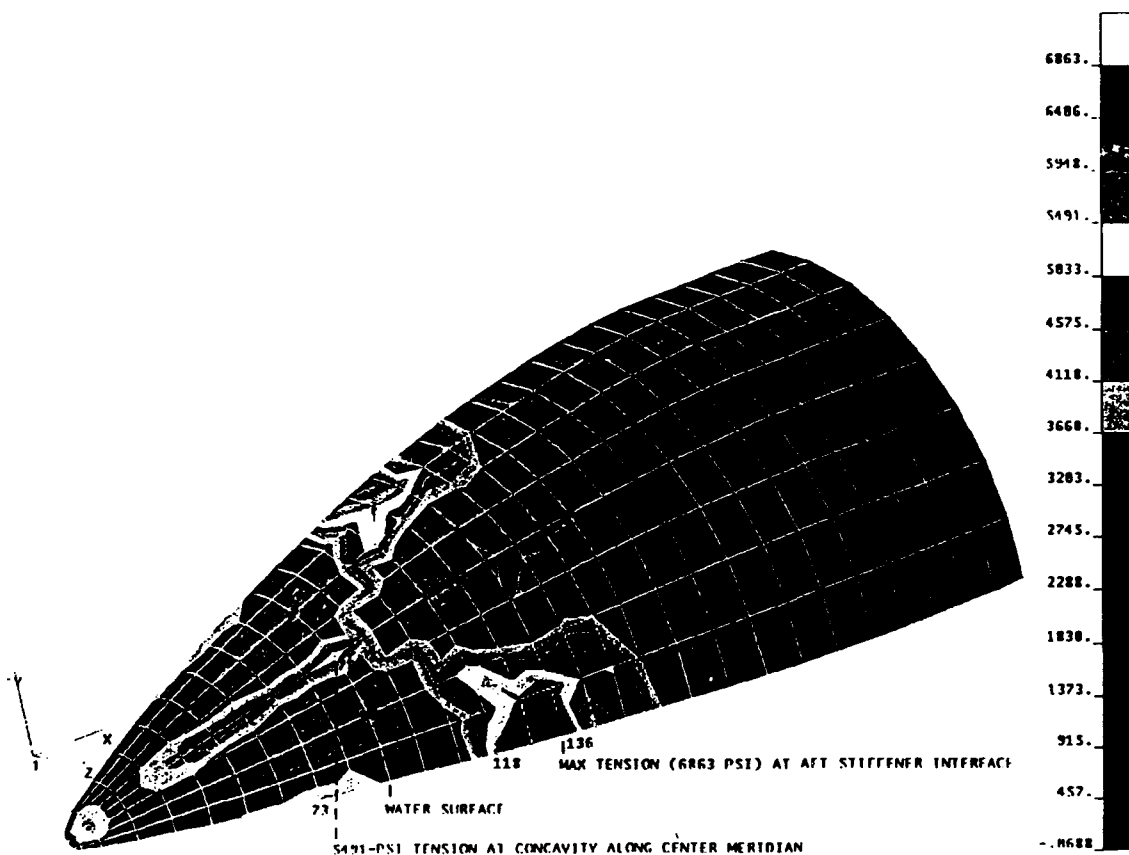
Figure 9b. Third principal stresss (s_3) of inner surface at t= 3.113 ms (step 10).
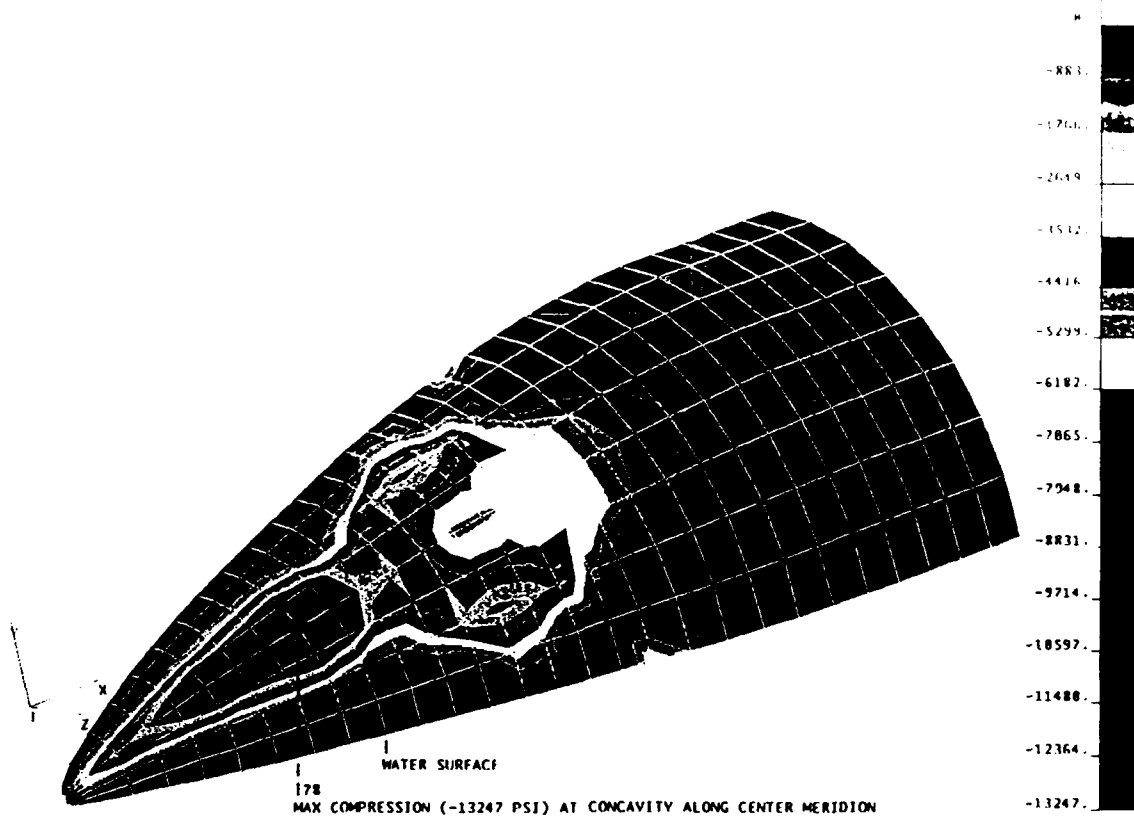
Figure 10a. First principal stresss (s_1) of outer surface at t= 3.113 ms (step 10).
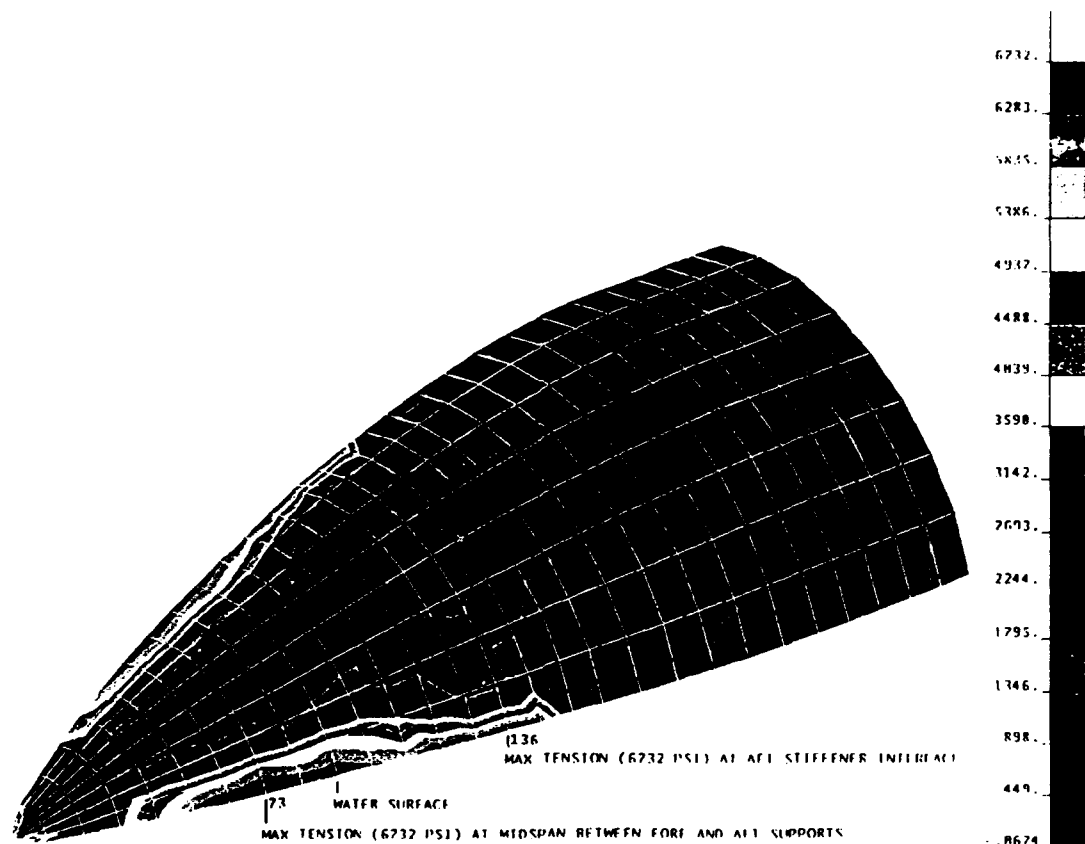
Figure 10b. Third principal stresss (s_3) of outer surface at t= 3.113 ms (step 10).
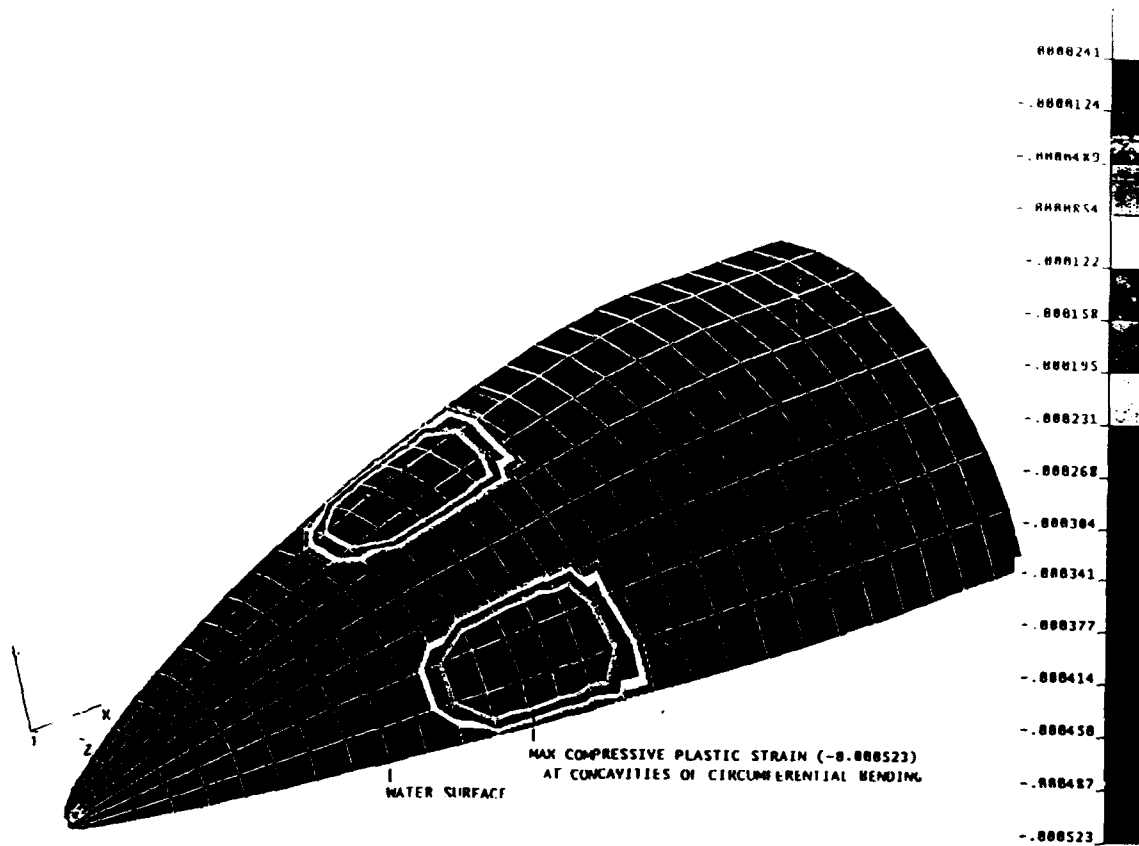
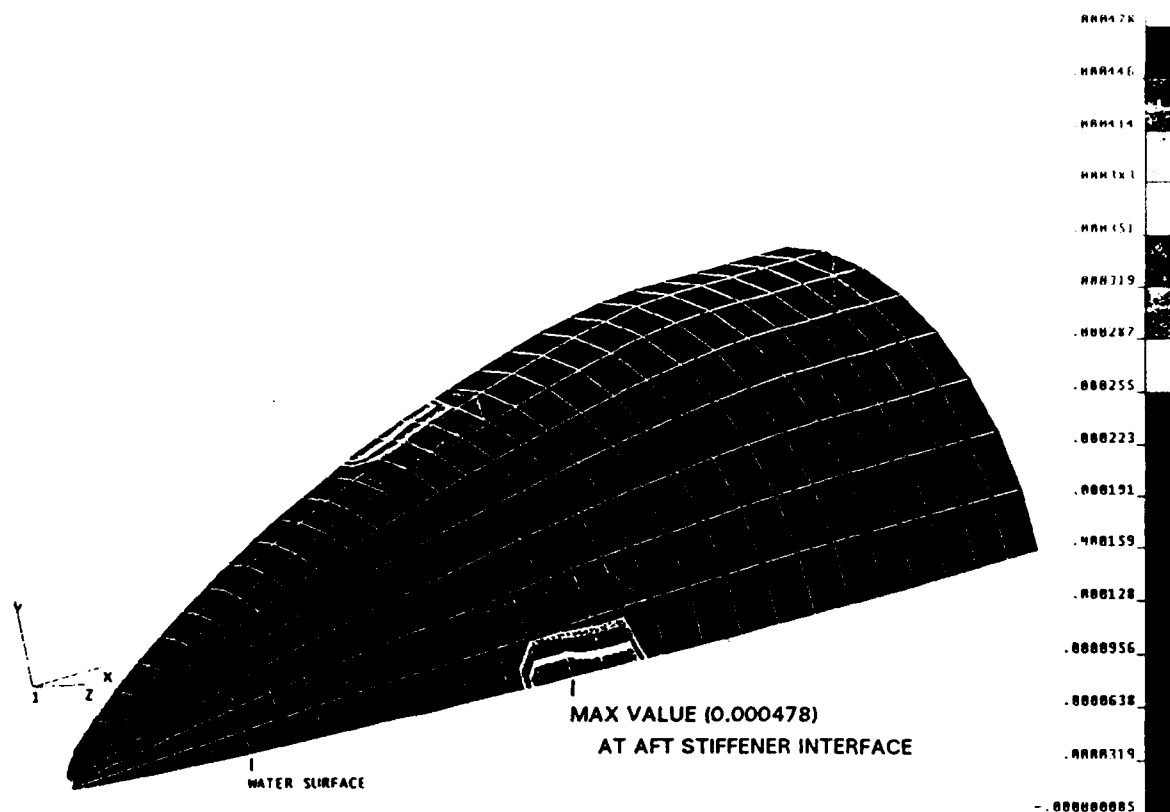Figure 11a. Meridional plastic strain (e^p_{11}) of inner surface at t= 3.113 ms (step 10).
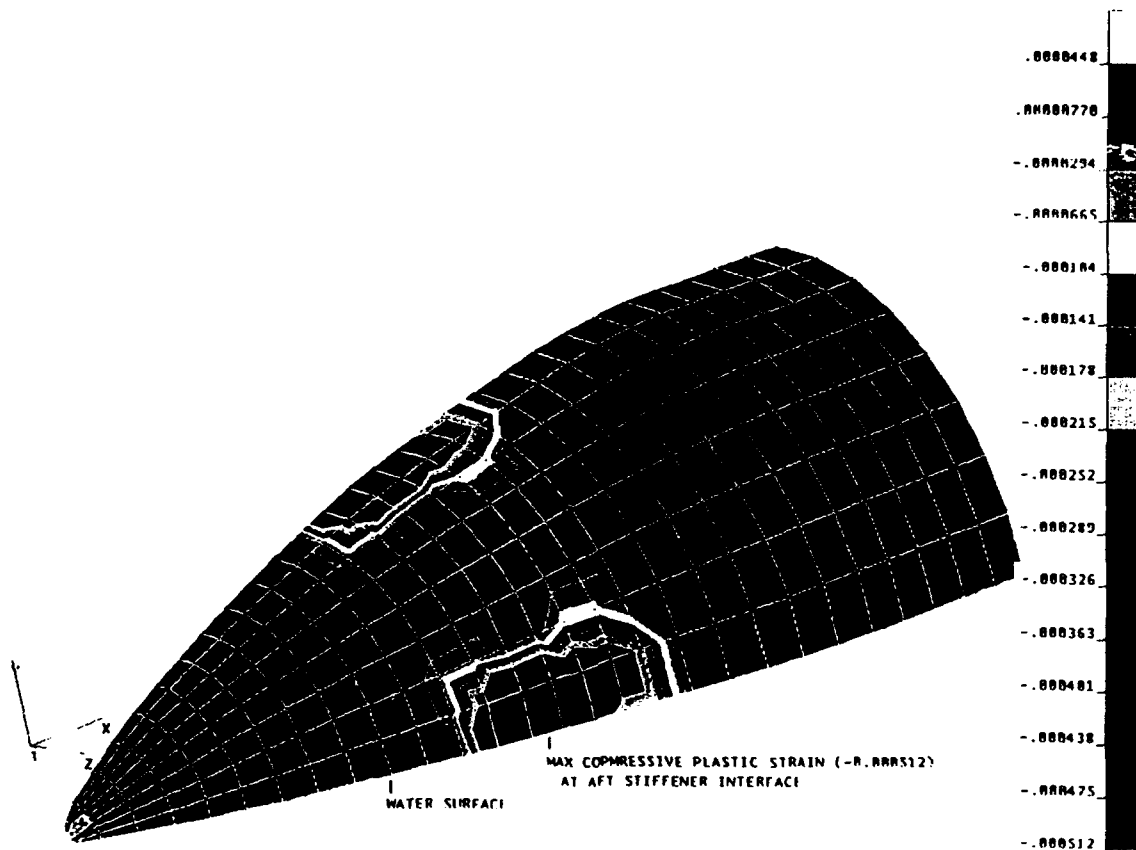
Figure 11b. Hoop plastic strain (e^p_{22}) of inner surface at t= 3.113 ms (step 10).
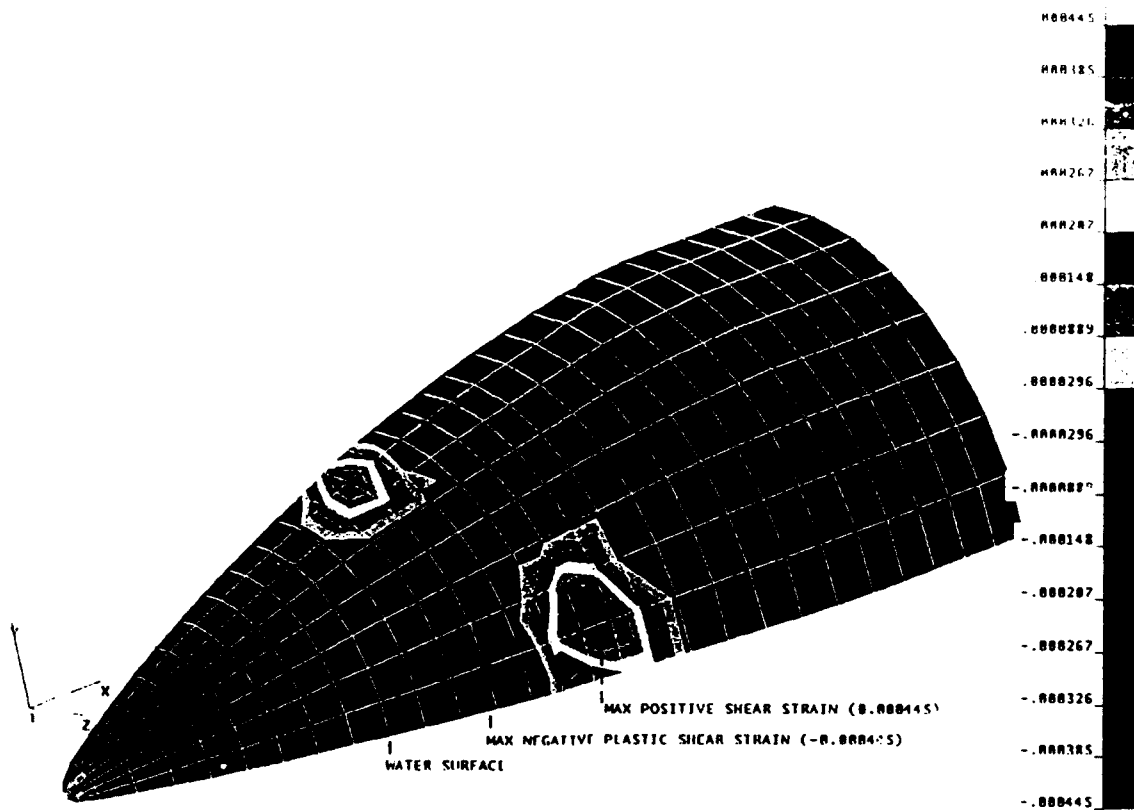
Figure 11c. In-plane plastic shear strain (e^P_{12}) of inner surface at t= 3.113 ms (step 10).
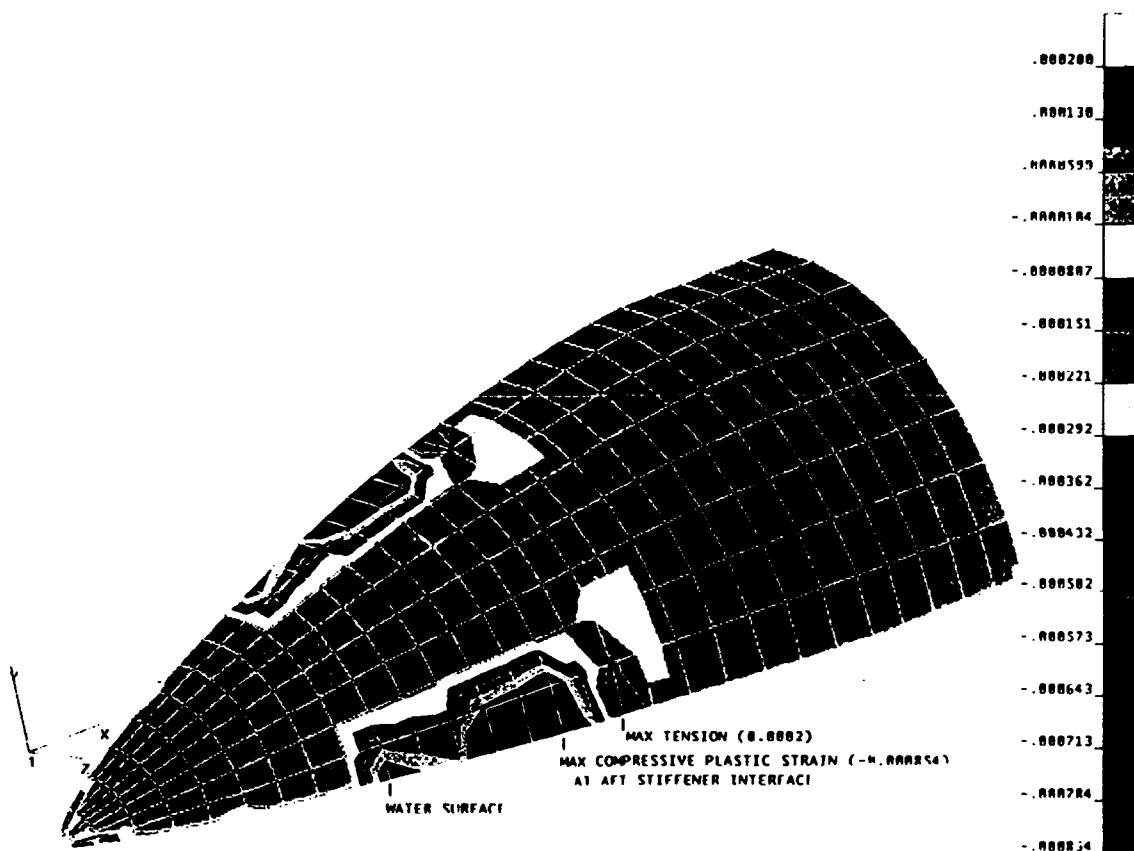
Figure 12a. Meridional plastic strain (e^P_{11}) of outer surface at t= 3.113 ms (step 10).
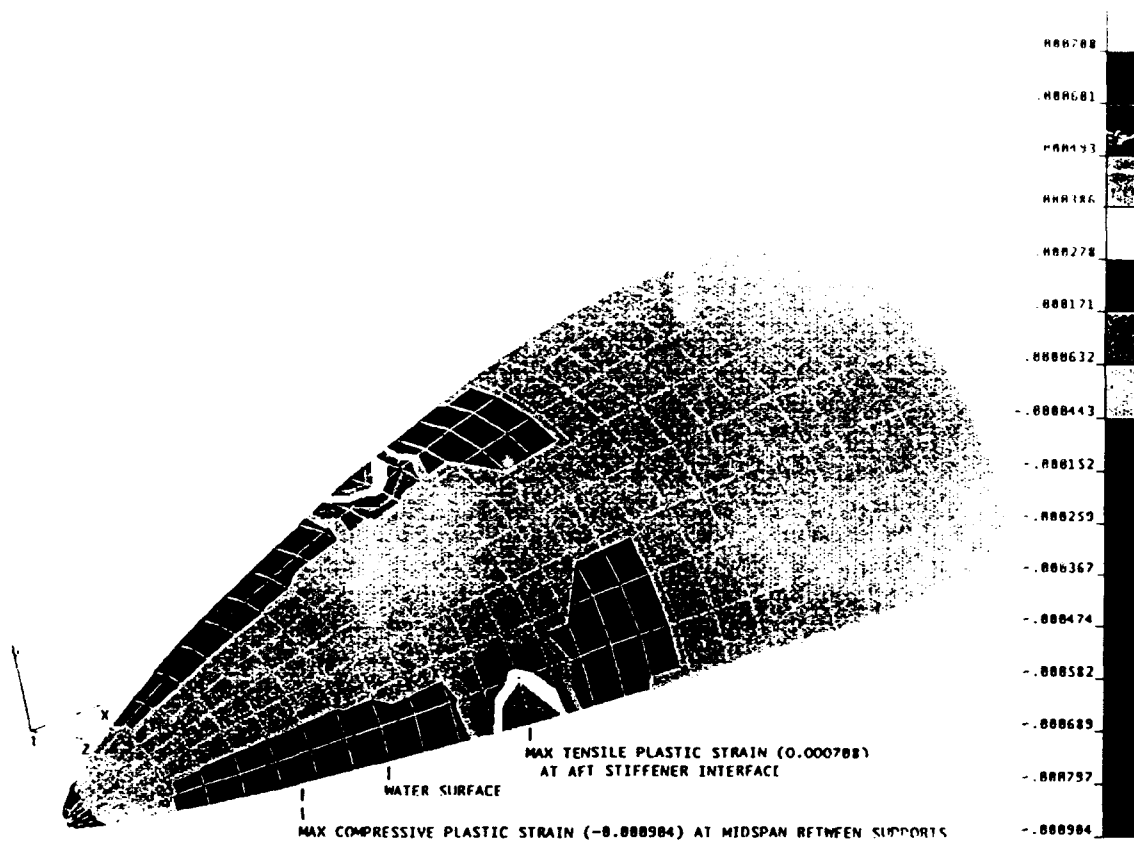
Figure 12b. Hoop plastic strain (e^P_{22}) of outer surface at t= 3.113 ms (step 10).
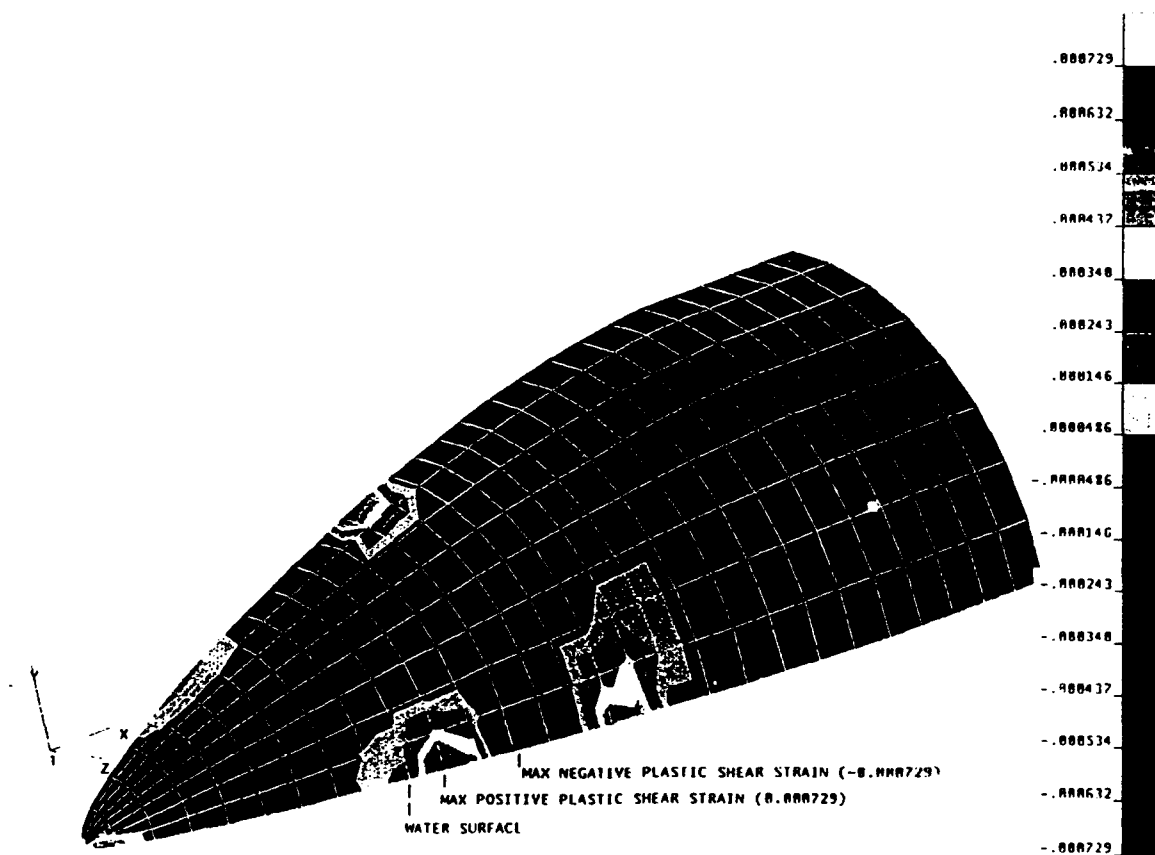
Figure 12c. In-plane plastic shear strain (e^P_{12}) of outer surface at t= 3.113 ms (step 10).

Figure 13a. Plastic strain magnitude of outer surface at t= 1.563 ms (step 6).
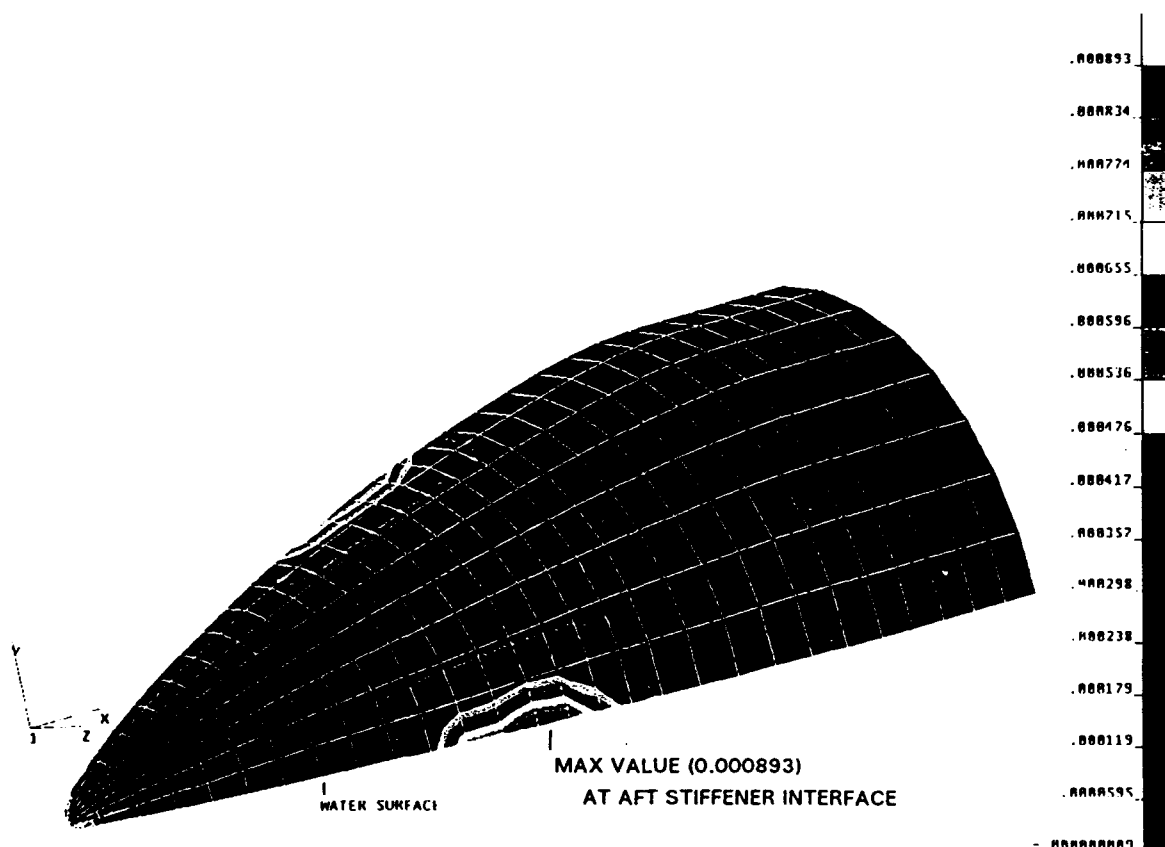
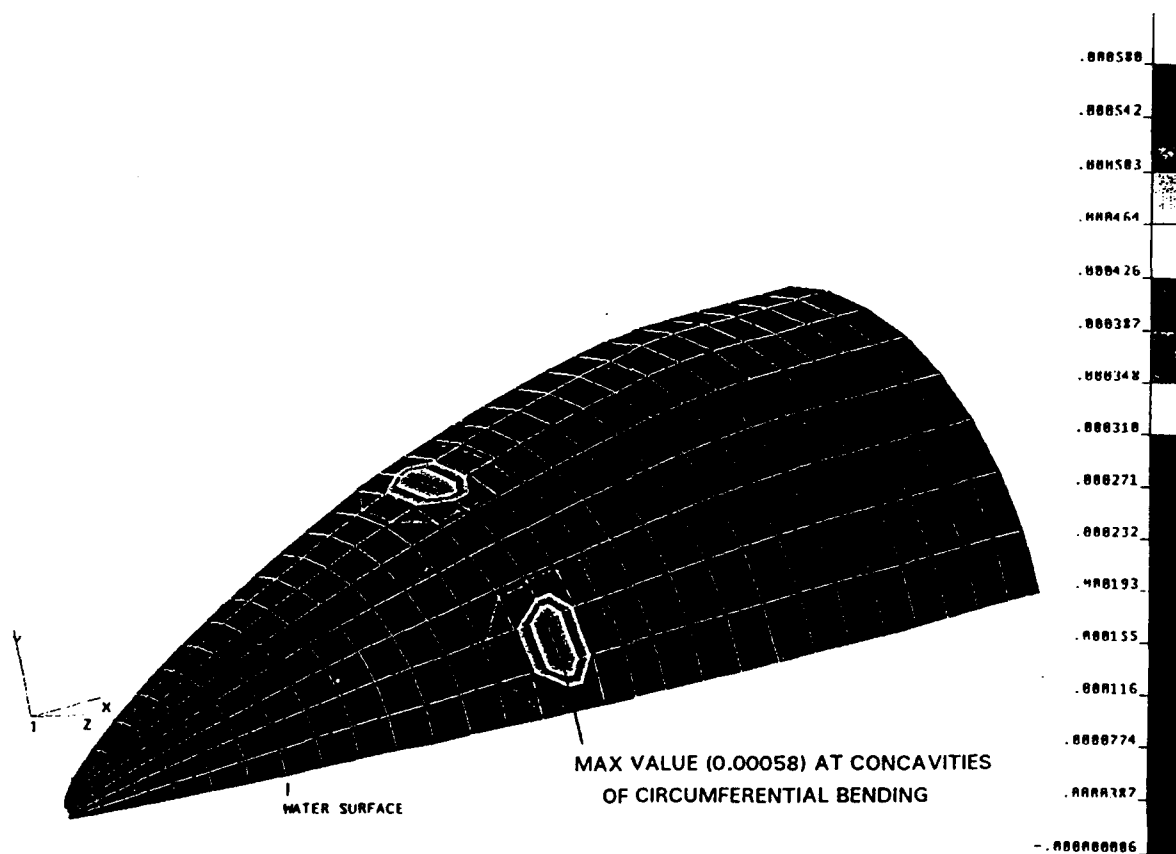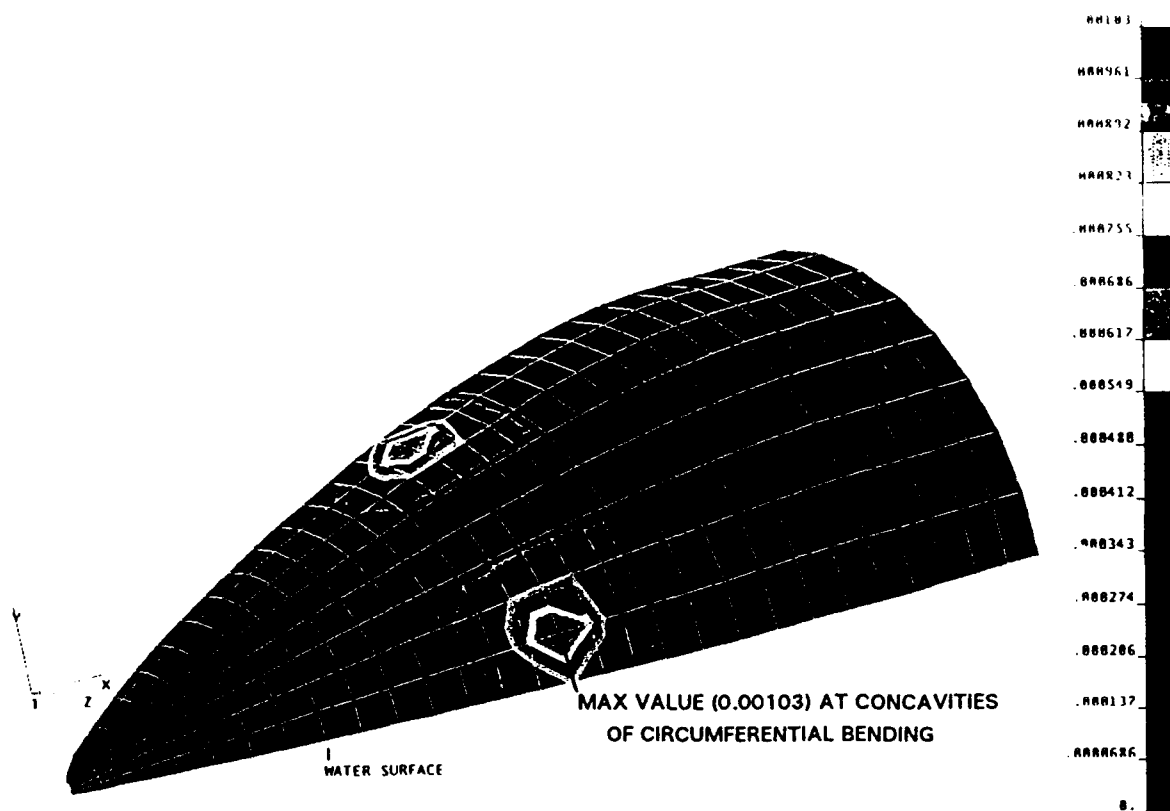Figure 13b. Plastic strain magnitude of outer surface at t= 2.323 ms (step 8).

MATER SURFACE

MAX VALUE (0.00105) AT MIDSPAN BETWEEN
FORE AND AFT STIFFENER INTERFACES
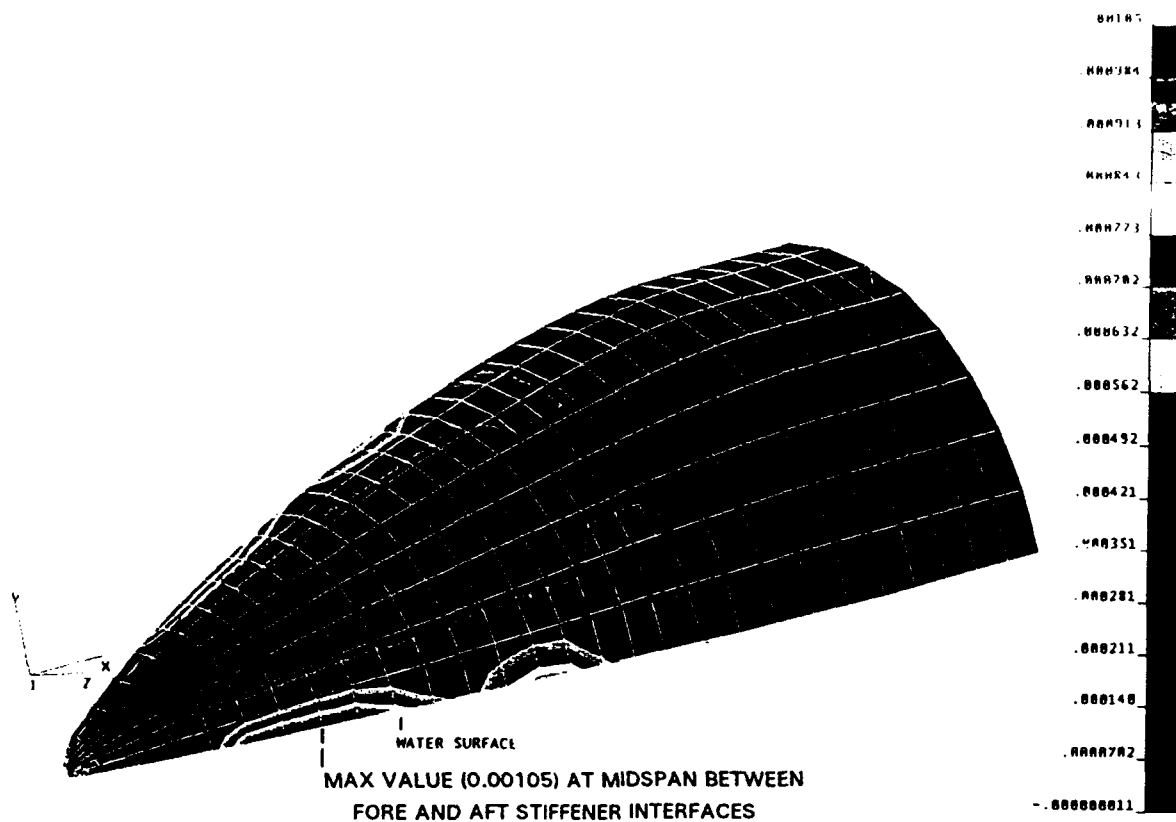
Figure 13c. Plastic strain magnitude of outer surface at t= 3.113 ms (step 10).

MAX VALUE (0.00058) AT CONCAVITIES
OF CIRCUMFERENTIAL BENDING

WATER SURFACE

Figure 14a. Plastic strain magnitude of inner surface at t= 1.938 ms (step 7).

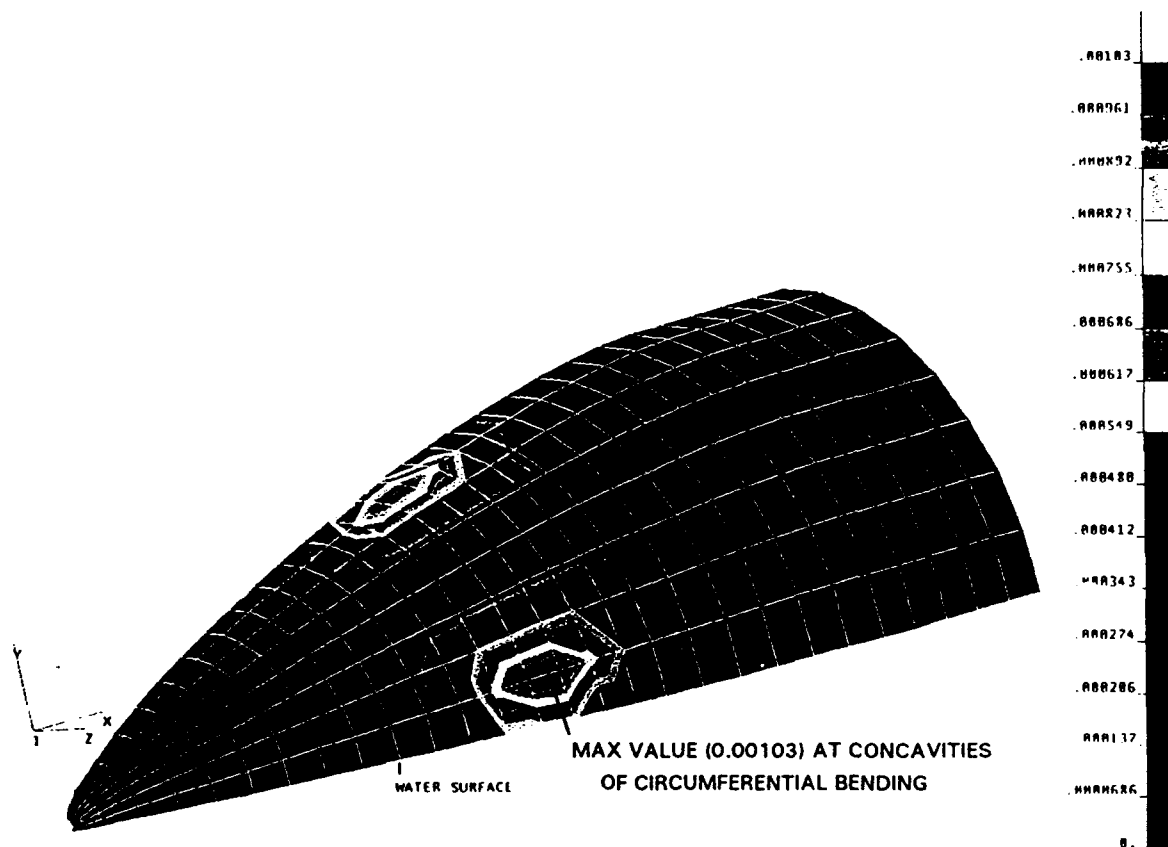Figure 14b. Plastic strain magnitude of inner surface at t= 2.323 ms (step 8).

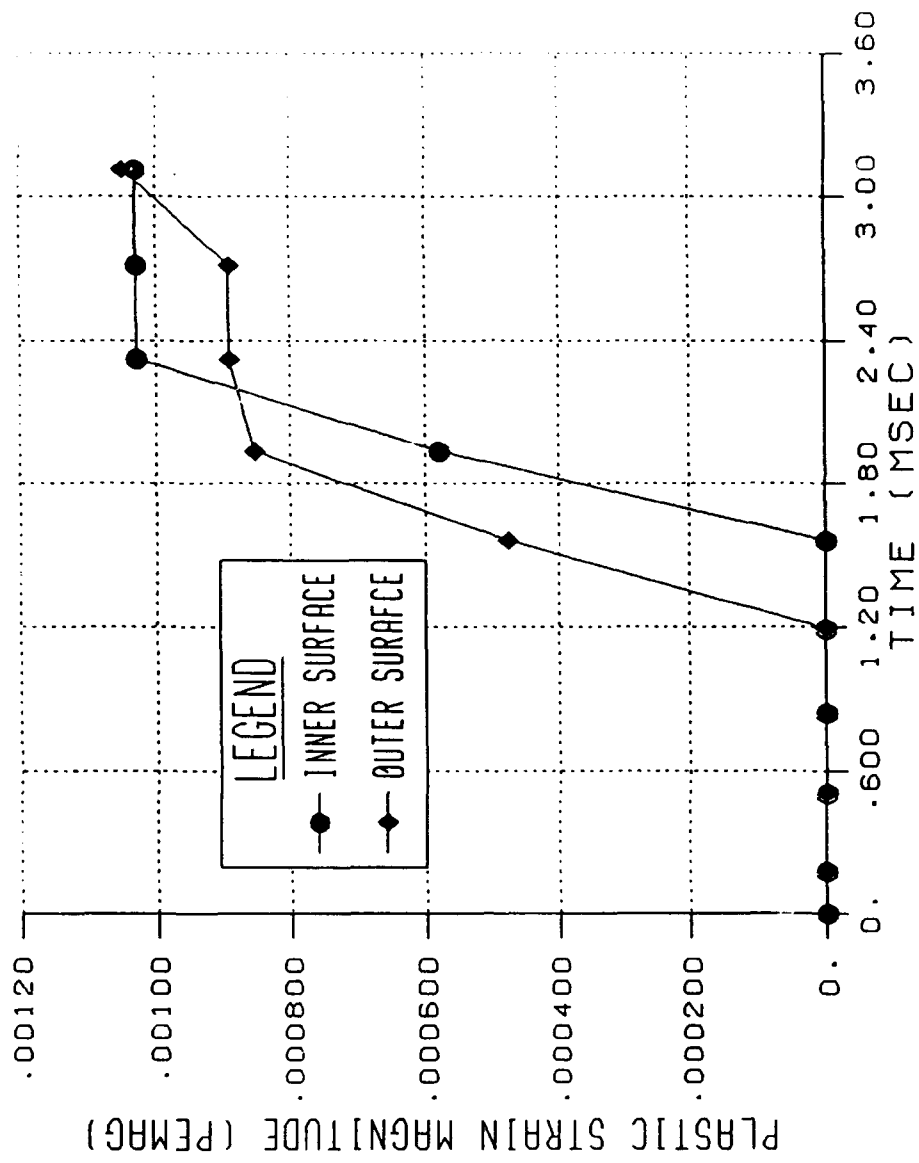Figure 14c. Plastic strain magnitude of inner surface at t= 3.113 ms (step 10).

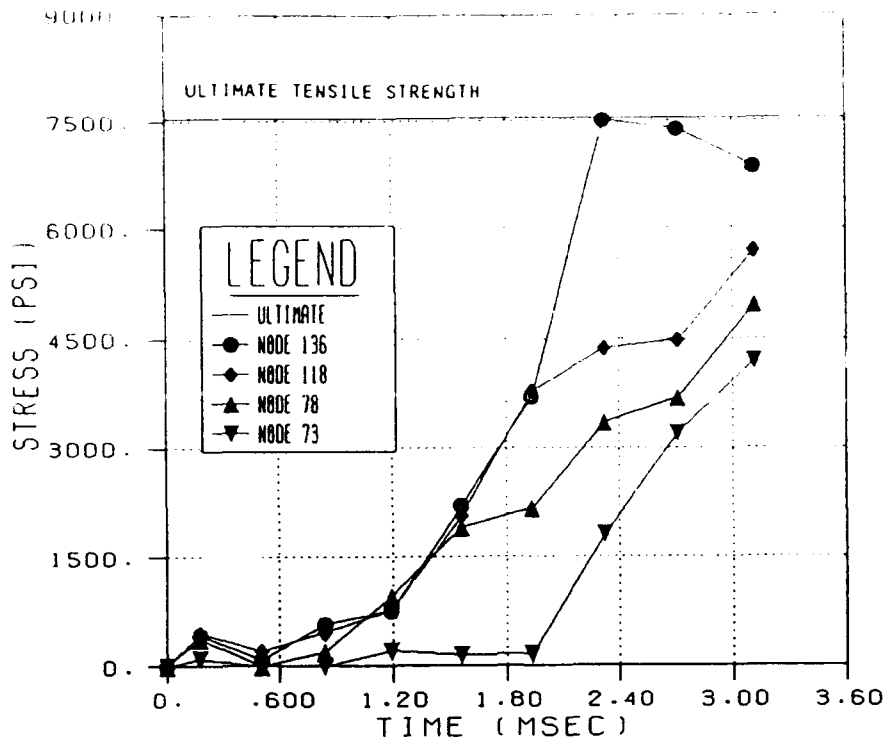Figure 15. Envelopes of plastic strain magnitudes for inner and outer surfaces.

28

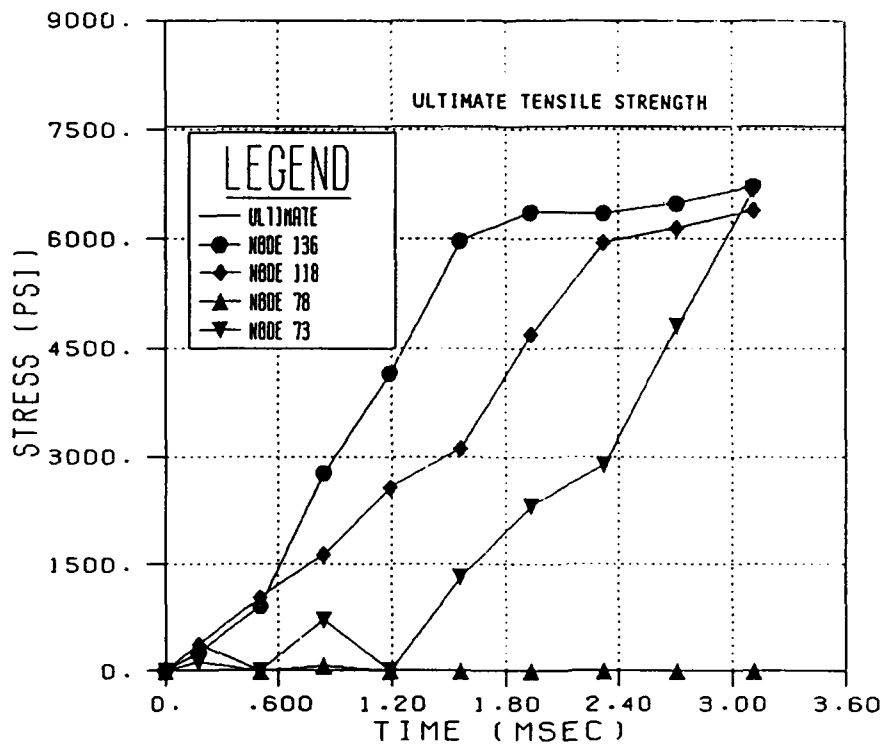Figure 16a. Third principal stress time-histories at inner surface.

Figure 16b. Third principal stress time-histories at outer surface.